

1 **This manuscript is a preprint:**

2 This manuscript has been accepted for publication by the Journal of Structural
3 Geology on May 14th 2024. Subsequent versions of this manuscript may differ slightly
4 in content following copyediting. The final version of this manuscript will be available
5 via the 'Peer-reviewed Publication DOI' link via this webpage when made available.

6

7 Please feel free to contact any of the authors directly or to comment on the
8 manuscript. We welcome feedback!

9 **Quantifying fault interpretation uncertainties and their impact on fault**
10 **seal and seismic hazard analysis**

11 Billy J. Andrews^{1*}; Zoë K. Mildon¹; Christopher A. L. Jackson²; Clare E. Bond³

12 1) School of Geography, Earth and Environmental Sciences, University of Plymouth,
13 Drake Circus, Plymouth, PL4 8AA, UK

14 2) Department of Earth Science & Engineering, Imperial College, Prince Consort Road,
15 London, SW7 2BP, UK

16 3) Department of Geology and Geophysics, School of Geoscience, Meston Building,
17 Aberdeen University, Aberdeen, AB24 3UE, UK

18 billy.andrews@plymouth.ac.uk Tel: +44 1752 600 600

19 Zoe.mildon@plymouth.ac.uk

20 c.jackson@imperial.ac.uk

21 clare.bond@abdn.ac.uk

22 Key words: Bias, Seismic reflection, Displacement analysis, Faults

23 **Acknowledgements**

24 We would like to thank DugInsight for the provision of an academic license for their
25 software package.

26 This work was supported by a UKRI Future Leaders Fellowship MR/T041994/1.

27 **Abstract**

28 Fault-horizon cut-off data extracted from seismic reflection datasets are used to study
29 normal fault geometry, displacement distribution, and growth history. We assess the
30 influence of three seismic interpretation factors (repeatability, measurement obliquity, and
31 fault cut-off type) on fault parameter uncertainty. Two repeat interpretations resulted in
32 mean differences of 5-15% for throw, 11-42% for heave, 9-31% for displacement, and 7-27%
33 for dip across faults. Measurement obliquity, where faults are interpreted using non-
34 perpendicular transects to fault strike, show increasing uncertainty with increasing
35 obliquity. Uncertainty in throw is 14-24% at obliquities $>20^\circ$ and 6-13% where obliquities
36 $<20^\circ$. Continuous cut-offs, including non-discrete deformation, generally exhibit greater
37 uncertainties compared to discontinuous (discrete) cut-offs. We consider the effect of
38 interpretation factors on fault parameters used in seismic hazard assessment (SHA) and
39 fault seal, using the established Shale Gouge Ratio (SGR). Even modest measurement
40 obliquities and repeatability errors can affect inputs for SHA, causing large differences in
41 throw- or slip-rate and inferred fault length. Measurement obliquity and repeatability have
42 a variable impact on SGR calculations, highlighting the additional importance of sedimentary
43 layer thickness and distribution. Our findings raise questions about the optimum workflow
44 used to interpret faults and how uncertainties in fault interpretation are constrained and
45 reported.

46 **1 Introduction**

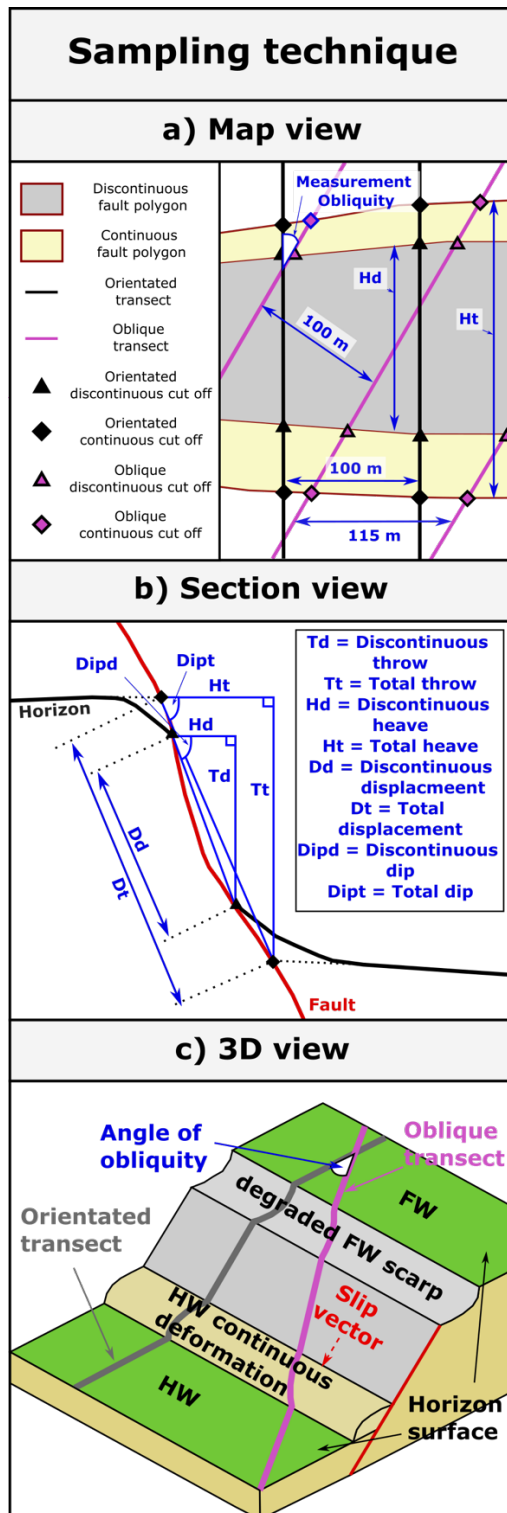
47 The measurement of horizon-fault cut-offs from seismic reflection datasets enables
48 extraction of key fault properties such as heave, throw and fault dip. Analysis of these
49 properties have advanced our understanding of fault geometry and evolution (e.g., Nicol et
50 al., 2005; Jackson and Rotevatn, 2013; Pan et al., 2021; Roche et al., 2021; Rodríguez-
51 Salgado et al., 2023), strain rate and its evolution in active and inactive rift systems (e.g.,
52 Meyer et al., 2002; Cowie et al., 2005; Marsh et al., 2010); and fluid-flow properties of faults
53 within hydrocarbon and/or CO₂ reservoirs (e.g., Yielding, 2002; Gibson and Bentham, 2003;
54 Yielding et al., 2011; Miocic et al., 2014). The use of horizon-fault cut-off data, combined
55 with well data, is routinely used to infer the sealing potential of faults cutting these
56 reservoirs. This is of particular importance for CO₂ storage projects (Klusman, 2003;
57 Amonette et al., 2010), where “appropriately selected and managed schemes” are expected
58 to retain 99% of injected CO₂ over a time period of 1000 years (IPCC, 2005). Fault cut-off
59 data can also be used to infer key parameters (e.g., slip-rate) to feed into fault based seismic
60 hazard assessments (e.g., fault dip, geological slip rate) (Nicol et al., 2005). Nuclear waste
61 disposal sites require geologically stable subsurface locations, and hence must be subject to
62 detailed seismic hazard assessment (Fenton et al., 2006; Connor et al., 2009; Mörner, 2013).
63 Where seismic data is involved in this assessment, any uncertainty in horizon cut-off’s at
64 faults could lead to uncertainties in the expected hazard at the site and therefore its
65 suitability for storing nuclear waste. It is therefore imperative to have confidence in
66 conclusions drawn from the analysis of fault properties extracted from seismic reflection
67 datasets and therefore, the uncertainties and biases associated with extraction of
68 underpinning data.

69 Uncertainties can be broadly classified as objective and subjective (Frodeman, 1995;
70 Tannert et al., 2007; Bond, 2015). Objective uncertainty, also known as “stochastic
71 uncertainty”, relates to the methods used for data acquisition, analysis, or interpretation of
72 the raw data (Tannert et al., 2007; Pérez-Díaz et al., 2020). In the case of seismic reflection
73 data, these include the velocity model used for the conversion between two-way-time to
74 depth (Schaaf and Bond, 2019; Faleide et al., 2021), the effect of compaction of fault
75 properties (Taylor et al., 2008), the spacing of picks during data extraction (Michie et al.,
76 2021; Robledo Carvajal et al., 2023), and whether the throw across a given fault exceeds or
77 falls below the limit of separability (Brown, 2011; Osagiede et al., 2014).

78 Subjective uncertainties pertain to biases and variability in results caused by the individual
79 analysing the data (Tannert et al., 2007); these include the geological interpretation and its
80 repeatability. Repeatability, which is the ability to replicate the data and interpretations of a
81 study, is recognised as a crucial aspect of any experiment (e.g., Goodman, 2016). Geology, in
82 particular, is susceptible to subjective uncertainty due to incomplete datasets and the lack
83 of consensus within the research community regarding key concepts and research methods
84 (Frodeman, 1995; Bond, 2015; Pérez-Díaz et al., 2020; Steventon et al., 2022; Magee et al.,
85 2023; Robledo Carvajal et al., 2023). For seismic reflection datasets, subjective uncertainties
86 can lead to multiple interpretations being drawn from the same seismic image (e.g., Bond et
87 al., 2007; Alcalde et al., 2017). Previous work has suggested that fault properties extracted
88 from seismic reflection data should have an error associated with them of between $\pm 5\%$
89 (Magee and Jackson, 2020a) and $\pm 10\%$ (Magee et al., 2023), however, no parametric studies
90 have been undertaken to date to test these essentially qualitative values.

91 Motivated by the discussion above, this paper considers the impact of two fault
92 interpretation workflow choices: measurement obliquity to fault-strike and interpreted fault
93 cut-off type (continuous, in which the horizon bends into the fault plane and discontinuous
94 in which the horizon cut-offs at faults are sharp). We also investigate the impact of
95 repeatability in fault interpretation for these workflow choices. Having, considered the
96 individual and compound uncertainties that result from these choices we examine the
97 impact on the fault properties: throw, heave, dip, and displacement; to show the relative
98 impact of each fault interpretation choice on properties that are used in risk and resource
99 assessment.

100 **2. *Expected sources of uncertainty in fault interpretation***



101

102

103

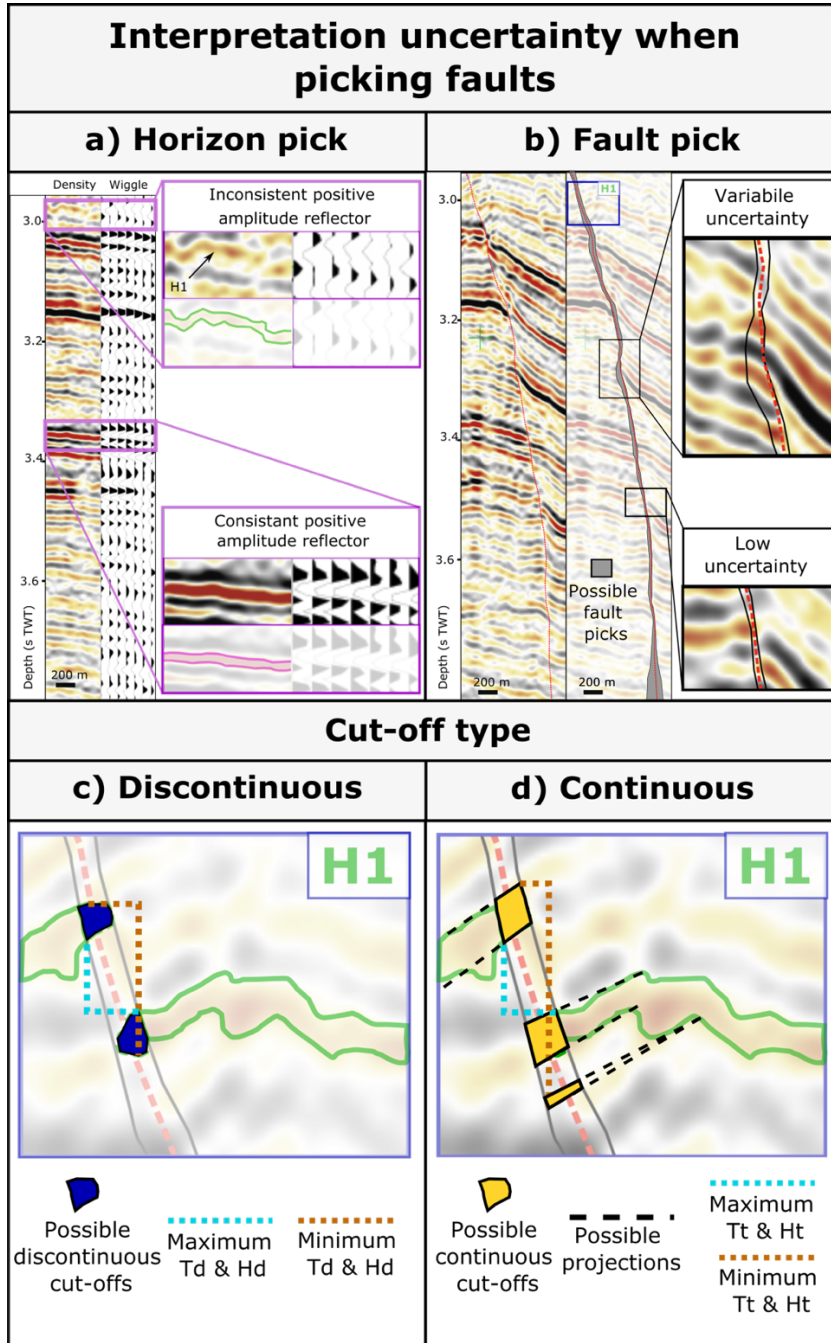
104

105

106

Figure 1: Sample strategy to assess obliquity errors when extracting data from fault cut-offs: a) Map view sample strategy and extracted parameters. Discontinuous and continuous fault polygons represent the horizon gap created by a fault, extending between the hanging wall and footwall for discontinuous and continuous cut-offs, respectively; b) Section view sample strategy and extracted parameters; c) 3D view showing the spatial difference between an orientated and oblique transect.

107 In this section we summarise the literature and theoretically expected contribution of each
 108 workflow choice on the repeatability of fault data extraction.



109

110 **Figure 2: Examples of expected interpretation uncertainty when picking fault cut-offs; a) quality of reflector**

111 **used to pick the horizon; b) quality of reflectors close to imaged faults; possible locations of c) discontinuous**

112 **and d) continuous fault cut-offs caused by uncertainties in horizon and fault picks.**

113 *Interpretation repeatability:* The repeatability of measurements from seismic reflection data
114 is influenced by human bias, leading to uncertainties in locating cut-offs (Schaaf and Bond,
115 2019). The position of cut-offs will be influenced by the interpreted horizon and fault, the
116 interpreted intersection point and any projection of regional dip onto the fault plane. These
117 factors are expanded upon below:

118 *Interpreted horizons (Figure 2a):* Horizons interpretations (picks) are made along
119 prominent reflections, ideally with consistent waveforms (Brown, 2011).
120 Inconsistent waveforms can result in high rugosity horizon picks, and ultimately
121 structure maps. These inconsistent wave forms are attributed to post-acquisition
122 processing or geological features (Chellingsworth et al., 2015). Auto trackers and
123 smoothing algorithms are commonly used to create geologically “reasonable”
124 horizons, with the choice of methods used introducing subjective uncertainty
125 (Brown, 2011; Chellingsworth et al., 2015). Previous studies have shown that horizon
126 picking uncertainties decrease near wells, potentially due to an increase in
127 interpreter confidence as the seismic reflection data is tied to data in the well
128 (Schaaf and Bond, 2019). Conversely, horizon picking uncertainties increase away
129 from wells, especially in areas of low seismic image quality and near faults (Alcalde
130 et al., 2017b; Schaaf and Bond, 2019). The image quality around faults can be
131 affected by the presence of a damage zone, which can vary in width based on fault
132 displacement and the structural position on the fault (Shipton and Cowie, 2003;
133 Childs et al., 2009; Choi et al., 2016). Furthermore, correlating horizons across faults
134 may be challenging due to variations in reflection properties, the presence of
135 footwall degradation (Bilal et al., 2020), and/or changes in seismic stratigraphy in the

136 footwall/hangingwall, and especially when reflectors cannot be traced around fault
137 tips (Bond et al., 2007; Bond, 2015; Chellingsworth et al., 2015). We anticipate
138 increased horizon picking uncertainty for faults with large displacement, at segment
139 boundaries/fault tips, or in locations where footwall degradation has occurred.

140 *Interpreted faults:* Uncertainties in fault placement are influenced by the strength of
141 seismic reflector and image quality (Alcalde et al., 2017b; Schaaf and Bond, 2019)
142 (Figure 2b). Interpretation uncertainty increases in areas with decreased reflector
143 strength (Schaaf and Bond, 2019). Strong seismic reflectors overlying or underlying
144 weak reflectors reduce uncertainty in our interpretation of the latter, and faults that
145 conformed to expected geometries (e.g., matching the regional trend) are more
146 reliably picked (Bond, 2015; Alcalde et al., 2017a; Schaaf and Bond, 2019).

147 *Interpreted horizon-fault intersection (i.e., cut-offs):* The way that reflections
148 (interpreted as horizons) intersect with faults, i.e. cut-offs, are open to interpretation
149 and therefore potentially uncertain. This arises, at least partly, from there being two
150 components of fault-related deformation; *discontinuous*, which results from brittle
151 strain accommodated by fault-slip and is imaged seismically by discrete off-set of
152 horizons across a fault; and *continuous*, which relates to folding (i.e., ductile strain)
153 and/or brittle deformation below the resolution of the seismic reflection dataset, in
154 which horizons are imaged in the seismic reflection data as bending into the fault. As
155 such, two types of cut-off can be measured: discontinuous cut-offs, and continuous
156 cut-offs (Figure 1b), which account for both the discontinuous and continuous
157 components of deformation (Childs et al., 2017; Delogkos et al., 2017, 2020). These
158 cut-offs can then be used to calculate fault throw, heave, dip, and displacement. The

159 inclusion or not of continuous deformation depends on the scientific objective and
160 the nature of the faulting. For example, to derive long-term fault slip-rates the
161 continuous portion of deformation is considered (Lathrop et al., 2021; Pan et al.,
162 2021). In contrast, only the discontinuous portion is required to calculate lithological
163 juxtapositions, shale gouge ratio and ultimately fault transmissivity.

164 Uncertainties affect cut-off types differently. Discontinuous cut-offs (Figure 2c), are
165 influenced by uncertainties in the position of the fault plane and horizon. Analysis of
166 fault cut-offs suggests that areas of low image quality are associated with large
167 uncertainty, as seismic image quality generally decreases with depth this also leads
168 to increased uncertainty with depth (Alcalde et al., 2017b; Schaaf and Bond, 2019).
169 Moreover, cut-offs on faults with low displacement near the limit of separability
170 (Magee et al., 2023) and the hanging wall cut-off of large displacement faults, which
171 are deeper and due to additional accommodation space often show changes in
172 seismic stratigraphy compared to the footwall (Alcalde et al., 2017b), are prone to
173 higher uncertainties. Continuous cut-offs require the regional dip of the horizon to
174 be projected onto the fault plane (Figure 2d). In cases of small-displacement faults
175 where continuous deformation comprises a significant portion of the displacement,
176 the interpreter must choose where the fault intersects the deflected horizon (Faleide
177 et al., 2021; Magee et al., 2023). This introduces uncertainty as there are multiple
178 feasible locations from which to project the horizon onto the fault plane, as well as
179 the position of the fault plane itself (Fig 2d). Where both types of deformation are
180 present (e.g., fault growth through a mixture of continuous and discontinuous
181 imaged deformation), the position of the fault plane will likely have lower

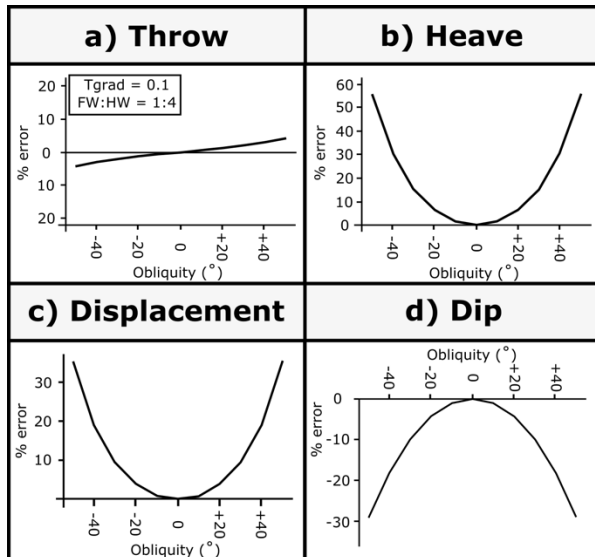
182 uncertainty, but the interpreter still needs to subjectively determine where the
183 regional dip of horizons transitions into near-fault continuous deformation.

184 Seismic image quality vertical exaggeration are common factors that influence subjective
185 uncertainties. To minimise their impact in our analysis, horizons at similar depths, with
186 similar resolutions, are selected and a consistent vertical exaggeration (~1:4) is used during
187 fault picking.

188 Previous studies have focused on the impact of subjective bias on data extracted from
189 multiple interpreters (Bond et al., 2007, 2012; Bond, 2015; Schaaf and Bond, 2019).
190 However, limited attention has been given to the consistency of an individual's
191 interpretation. Magee et al. (2023) conducted a study where an individual made repeat
192 picks on the same horizon of a low-displacement fault, revealing variations in fault cut-off
193 positions that affected the extraction of throw and heave. Nevertheless, the datasets were
194 found to be statistically equivalent and exhibited lower uncertainty compared to another
195 interpreter's interpretation of the same horizon. Similar 'internal consistency' within
196 individuals interpretations has also been observed in the field classification of faults and
197 fractures (Andrews et al., 2019; Shipton et al., 2020) and seismic reflection-based models
198 (Alcalde and Bond, 2022). This study aims to build on these findings by investigating the
199 magnitude of individual internal consistency in fault properties, examining variations across
200 different horizons, faults, cut-off types and measurement obliquity.

201 *Measurement obliquity:* Measurement obliquity is the angle relative to the fault strike that
202 fault and fracture properties are sampled (Figure 1a), and it can affect the extraction of key
203 properties such as spacing and dip (Terzaghi, 1965; Watkins et al., 2015). Optimal fault

204 interpretation strategies involves sampling using transects that are perpendicular to fault
 205 strike. For true normal faults, this is parallel to the slip vector; for all faults measuring fault
 206 dip strike perpendicular avoids measuring an apparent fault dip.



207
 208 **Figure 3: Theoretical % error across a range of oblique transects for a) throw, b) heave, c) displacement and**
 209 **d) dip assuming a fault dip of 40°. For throw, a throw gradient of 0.1 and a FW:HW displacement ratio of 1:4**
 210 **was assumed. The shape of the theoretical % error graphs implies that heave, and therefore displacement**
 211 **and dip, will have a high theoretical error at high obliquity, whereas throw will have a lower theoretical**
 212 **error.**

213 The theoretical error on the extracted fault parameters can be estimated by considering the
 214 change in cut-off position caused by an oblique sample line (Fig 3). For a fault with 40° dip,
 215 throw errors remain low even at high measurement obliquities (Fig 3a). However, heave
 216 errors exceed 50% at measurement obliquities of ±50° and exceed 10% at an obliquity of
 217 ~25°. These errors would lead to moderate over- and under-estimates of displacement and
 218 dip, respectively, where measurement obliquity exceeds 20° to 30°. Below ~20°, theoretical
 219 error estimates suggest that obliquity will have a limited effect on the extraction of fault
 220 parameters (Fig 3). Therefore, we expect measurement obliquity to have a small effect on

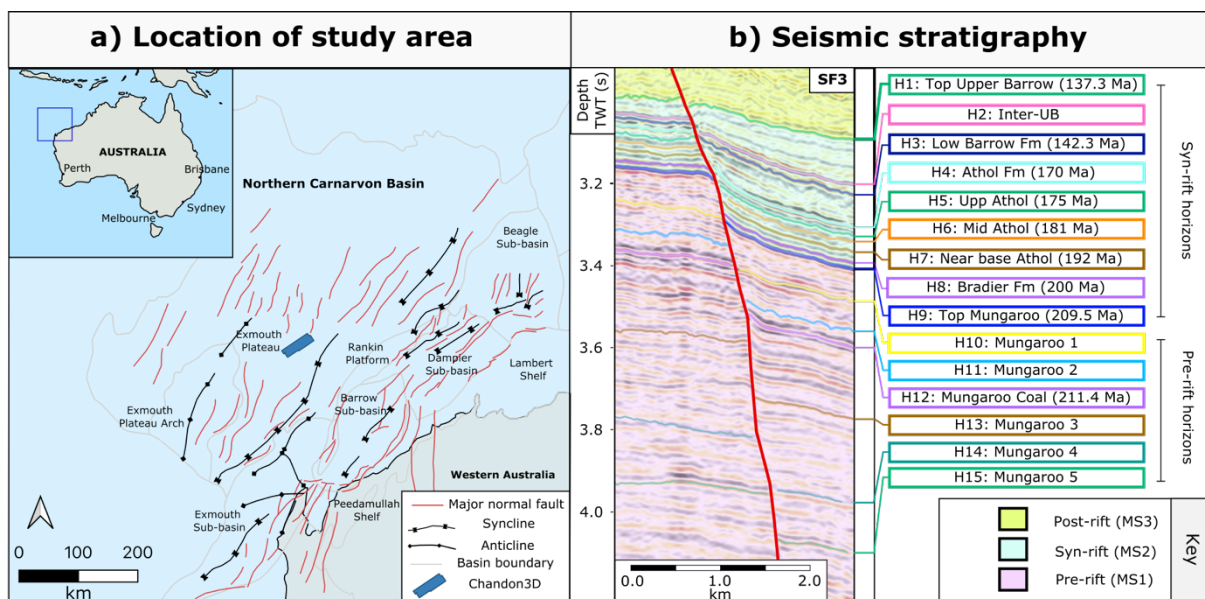
221 the extraction of throw (Fig 3a), but greatly impact measurements of heave (Fig 3b), and
 222 therefore displacement and dip (Fig 3c, d).

223 It is not always possible to sample faults using strike perpendicular transects. This is due to
 224 the non-linear morphology of faults and the scale-dependant nature of strike. To use strike
 225 perpendicular transects along the length of a fault may be time intensive, and the way in
 226 which data is combined between different transect orientations could casuse errors in
 227 subsequent analysis. Furthermore, if 2D seismic lines are the only available datasets, the
 228 lines may not be optimally orientated (i.e., perpendicular) to local fault strike. This study
 229 aims to investigate the threshold at which measurement obliquity significantly affects the
 230 extraction and interpretation of fault properties, and therefore to provide quantified errors
 231 that can be applied to other studies.

232 **3 Dataset and methods**

233 **3.1 Seismic data**

234

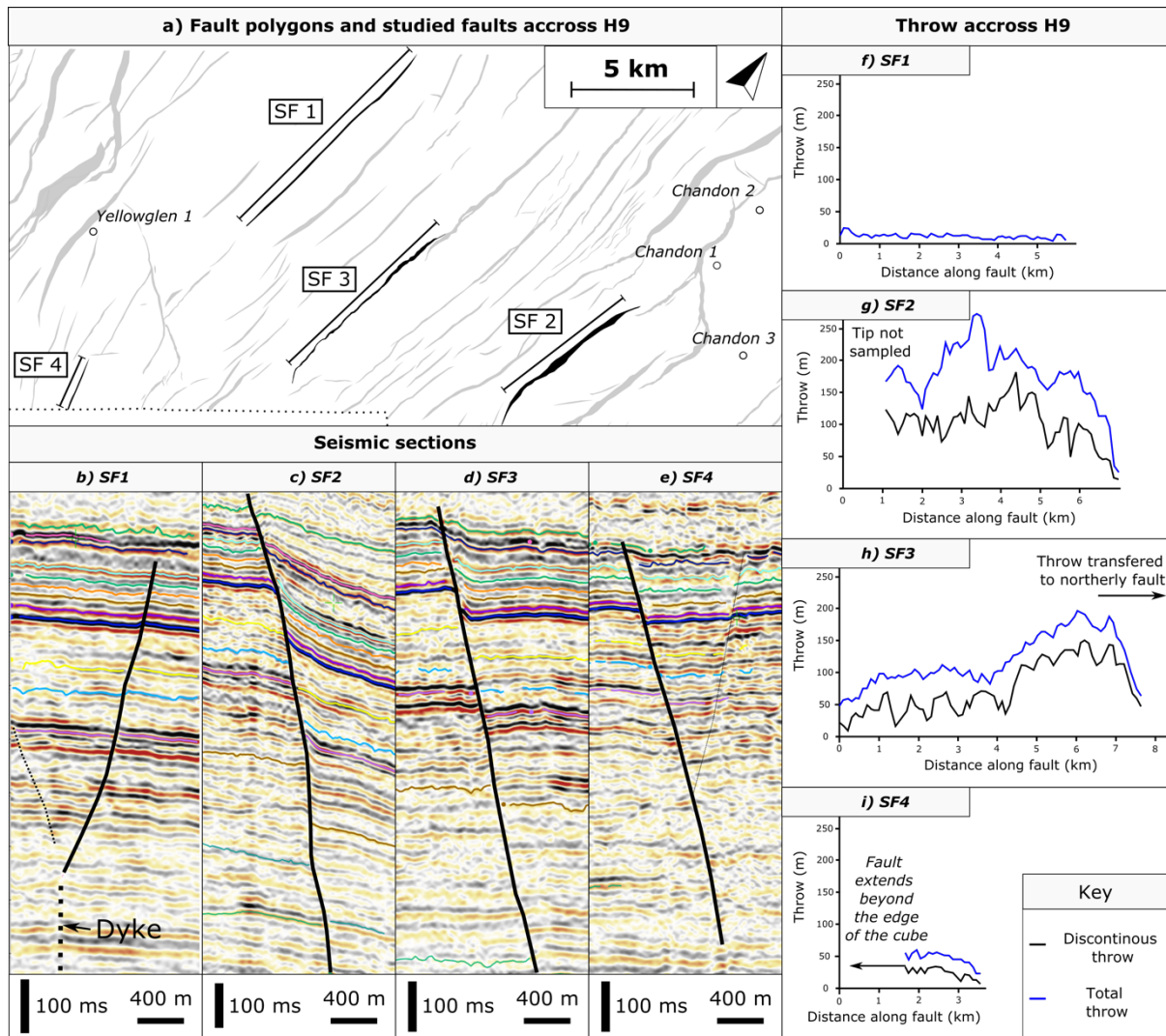


235 **Figure 4: Regional geology and seismic stratigraphy: a) Overview of the North Carnarvon Basin showing**
236 **the major faults and sub-basins (adapted from Bilal and MacClay, 2021). The study area, as marked as a blue**
237 **box, is not located on one of the major faults and as such displays little footwall degradation compared to**
238 **other faults in the area; b) Seismic stratigraphy highlighting the key horizons used in this study. MS refers**
239 **to the megasequences referred to in Bilal and McClay (2022).**

240 We use a high-resolution 3D seismic survey (Chandon3D) located on the Exmouth Plateau,
241 offshore NW Australia (Fig 4). Chandon3D is a time-migrated, zero-phase survey that has a
242 length of 6 seconds two-way time (TWT) and bin-spacing of 25 m. The data are displayed
243 with a SEG reverse polarity, i.e., a downward increase in acoustic impedance corresponds to
244 a trough (black) reflection, and a downward decrease in acoustic impedance corresponds to
245 a peak (red) reflection (Figure 2a). We used four wells to constrain the age and lithology of
246 the interpreted horizon reflections (Chandon-1, Chandon-2, Chandon-3, Yellowglen).

247 We estimate seismic velocities using time-depth plots derived from check-shot data
248 obtained from nearby wells (Supplementary 2). Since the interval of interest (~2.9s to 4.1s
249 TWT) extends below the depth of the wells (2093 m, 3.324s TWT), we extrapolated seismic
250 velocities through this interval by fitting a second-order polynomial to the combined check-
251 shot dataset. Differences in polynomials between individual wells introduces depth-
252 dependant uncertainty (Supplementary 2); however, given the similar depth of cut-offs
253 across all faults and the moderate- to low-throw magnitude, any absolute errors in depth
254 should be consistent between picks at a given location on the fault. Differences in our
255 analyses are therefore caused by obliquity, fault cut-off choice and interpretation and
256 repeatability errors.

257 The resolution of an interval of interest in a seismic cube can be estimated by calculating the
258 limits of seperability and visibility respectivey (Brown, 2011). The limit of sperability
259 corresponds to the minimum vertical discance whereby interfaces will prodice two distinct
260 seismic reflectors, and the limit of visibility the vertical distance whereby interfaces are
261 indistinguishable from background noise (Brown, 2011). Between these values, individual
262 reflectors cannot be resolved and they will appear as a tuned reflection package (Brown,
263 2011) (i.e., no discontinuous deformation will be visible). To calculate the limits of
264 seperability and visibilty, we extract the domant frequencies (f) and average interval
265 velcoities (v) for the shallowest (2.9 to 3.1 s TWT) and deepest (3.9 to 4.1 s TWT) intervals
266 analysed in our study. From these we calculate the dominant wavelength (λ) for the interval
267 of intrest ($\lambda = v/f$) and then calculate the limit of seperability ($\sim\lambda/4$) and visibility ($\sim\lambda/4$)
268 (Brown, 2011). Our calculations indicate that the limit of seperability and visibility at the top
269 of the the studied section are ~ 17 to 21 m and 2 to 3 m respectively, and at the base of the
270 studied section, these values increase to ~ 60 m and ~ 8 m (see Supplementay 2 for
271 calculations). This resolution is sufficient to enable the investigation of small errors in our
272 analyses caused by the three elements of interpretation uncertainty we are interested in.



274

275 **Figure 5: Studied faults:** a) fault polygons for Horizon H9, highlighting the location of the four quasi-straight
 276 faults studied; b-e) strike-perpendicular transects for each fault showing the structural style of each fault; f-
 277 i) along-strike profiles depicting the throw extracted using discontinuous (black) and continuous (i.e., total
 278 throw) (blue) cut-offs across the H9 horizon for data extracted using a strike-perpendicular transect. Note
 279 that the difference between the two lines represents the magnitude of deformation accommodated by
 280 folding and/or sub-seismic scale faulting.

281 The study area is situated in the Exmouth Plateau region of the Northern Carnarvon Basin,
 282 offshore NW Australia (Figure 4a). The region experienced several phases of rifting from the

283 Late Carboniferous to the Early Cretaceous (Tindale et al., 1998; Stagg et al., 2004; Direen et
284 al., 2008). The Triassic to recent tectono-stratigraphy of the Exmouth Plateau can be divided
285 into four main megasequences (Fig 4b) (Bilal and McClay, 2022). The main phase of WNW-
286 directed extension, which is associated with deposition of Megasequence-II, resulted in the
287 formation of north-south striking normal faults, including three of the four faults we focus
288 on (SF1, 3, 4) (Figure 5) (Stagg et al., 2004; Bilal et al., 2020; Bilal and McClay, 2022). During
289 rifting, the basin was sediment-starved, meaning it now contains a relatively condensed
290 ($\lesssim 100$ m thick) of a largely marine syn-rift succession (Karner and Driscoll, 1999). This
291 succession is separated from the overlying Late Jurassic marine Dingo Claystone by the end-
292 Callovian regional unconformity (Tindale et al., 1998; Yang and Elders, 2016; Bilal et al.,
293 2020; Bilal and McClay, 2022). Tectonic faulting slowed, or stopped, during the Late Jurassic,
294 but resumed after formation of the regional unconformity (~ 148 Ma), being synchronous
295 with the deposition of the Barrow Group (~ 148 to 138 Ma) (Gartrell et al., 2016; Reeve et
296 al., 2016; Paumard et al., 2018). During the second phase of faulting, new N-S to NW-SW
297 striking, low-throw (< 0.1 km) normal faults developed (Black et al., 2017), with some of the
298 earlier faults being reactivated (Bilal and McClay, 2022). Continental breakup occurred
299 during the Early Cretaceous (~ 135 to 130 Ma) and was followed by thermal subsidence and
300 passive margin development (Robb et al., 2005; Direen et al., 2008; Reeve et al., 2021).

301 In addition to tectonic faults, a series of dyke-induced faults are identified across the study
302 area (Magee and Jackson, 2020b, 2020a; Magee et al., 2023), of which SF2 (Fig 5b) is an
303 example. These dykes are expressed as sub-vertical, low-amplitude zones that disrupt the
304 seismic reflectors within the pre-rift sedimentary succession (Magee and Jackson, 2020b).
305 Several associated grabens occur directly above and along the dykes, bound by oppositely

306 dipping faults that intersect with the upper dyke-tip (Magee and Jackson, 2020b, 2020a).
307 These dyke-induced faults are often long (10s km), show variable dip and displacement
308 distributions along strike, typically have low maximum throw values (often <50 m), and
309 terminate upwards at the Base Cretaceous unconformity (Magee and Jackson, 2020b,
310 2020a; Magee et al., 2023).

311 Four sub-linear faults (SF1-4) were analysed in this study, varying in length from 2.4 to 7.9
312 km and exhibiting maximum total throw (i.e., throw extracted using continuous cut-offs)
313 ranging from 32 to 273 m (Fig 5f-i). Discontinuous and continuous cut-offs can be measured
314 for faults SF2-4; however, the average throw across SF1 (13 ± 6 m) is between the limit of
315 separability and visibility for the seismic cube. Therefore, only a small number of picks along
316 this fault display discontinuous throw. We report only data extracted from continuous cut-
317 offs for this fault. It is also expected that greater uncertainty will be observed for this fault
318 due to the lack of discrete deformation to guide cut-off picking (Magee et al., 2023). Figure
319 5f-i shows the throw distributions of the base syn-rift horizon (H9), showing variations
320 between faults. Along Horizon 9, faults exhibit moderate dips ($52^\circ \pm 8^\circ$) with lower dips
321 observed at shallower depth, within the syn-rift succession ($H1 = 32^\circ \pm 6^\circ$).

322 The studied faults have been buried beneath a thick layer of post-Cretaceous sediments,
323 which can lead to compaction and rotation of pre-existing structures to shallower dips
324 (Allen and Allen, 2013). Burial-related compaction will also act to reduce the throw across
325 syn-sedimentary faults by <15% in sand-shale mixed lithologies (Taylor et al., 2008) similar
326 to those observed in the study area (Bilal and McClay, 2022). However, decompaction was
327 not performed in this study due to uncertainties in decompaction parameters, particularly
328 for more deeply buried hanging wall sediments not sampled by well data. As a result, the

329 extracted values of fault throw, dip and displacement represent minimum estimates. Since
330 all faults have been buried to a similar depth, the impact of compaction on the extracted
331 fault properties should be consistent across the datasets, and thus should not affect our
332 statistical analysis or related conclusions.

333 **3.3 Sample strategy**

334 Oblique transects, relative to fault strike, were created close to the location of maximum
335 fault throw for each fault. The transects were created at obliquity intervals of 10° from
336 perpendicular (0°) to the faults at this point. This resulted in 11 transects, at different
337 obliquities (i.e., from 0° to $\pm 50^\circ$; Fig 1a) for each fault. Each transect was then transposed to
338 parallel positions along each fault at a separation of 100 m (following the strategy shown in
339 Fig 1a). This means that for the oblique analysis, the along-strike distance between adjacent
340 cut-offs is > 100 m (~ 156 m for 50° obliquity) and the exact location on the fault the data is
341 collected from differs between transects of different obliquity.

342 At each sample location (i.e., every transposed position where the fault is exposed along
343 each transect for each angle of obliquity), we collected discontinuous and continuous cut-
344 off data for 8-13 horizons, the actual number in each instance is determined by the regional
345 continuity of mapped reflectors. For discontinuous cut-offs, we identified the location
346 where the horizon intersects the fault in the footwall and hanging wall; for continuous
347 deformation, we projected the regional horizon dip onto the fault plane (Fig. 1b). Depth
348 values were converted from two-way travel time (TWT) to metres, and the following fault
349 properties were calculated: throw, heave, dip, and displacement (Fig. 1a, b). For dip and
350 displacement, we assumed that the slip vector is dip-parallel (cf. Magee and Jackson,

351 2020a). Where both discontinuous and continuous cut-offs are extracted (SF2-4), we also
352 calculated the ratio between the different types of throw.

353 To test the repeatability of interpretation, and the impact on fault properties, picks of
354 horizon H9 and H12 were repeated. These horizons were selected as their seismic reflection
355 characteristics are similar, and because both horizons could be correlated across the study
356 area. Fault interpretations were undertaken by a single interpreter (lead author Andrews) to
357 ensure no inter-interpreter bias (e.g., Magee et al., 2023). There was a minimum period of
358 three months between fault interpretations to reduce observations made during
359 interpretation 1 directly affecting the 2nd interpretation. Andrews has 2 to 3 years
360 experience of interpreting faults and picking fault cut-offs; familiarisation with the seismic
361 cube increased during the study, with continued interpretation. Whilst experience has been
362 shown to effect seismic interpretation (Bond et al., 2007; 2015); other studies (e.g., Magee
363 et al., 2023) show that interpretation by the same individual, resulted in fault data of a
364 similar magnitude to that derived from interpretations of the same dataset, completed by
365 interpreters with a range in experience of up to >10 years.

366 To facilitate the plotting and comparison of data between oblique and strike-perpendicular
367 transects, we determine the equivalent sample location of the cut-offs relative to the strike-
368 perpendicular transect. For oblique cut-offs, the equivalent strike-perpendicular sample
369 location will differ for the footwall and hanging wall (Fig 1a). To account for this, we take an
370 average of the two cut-offs to obtain the equivalent strike-perpendicular sample location on
371 the fault.

372 **3.4 Data presentation and statistical analysis**

373 We analyse and present our data on discontinuous vs continuous fault cut-off choice,
374 transect obliquity and interpretation repeatability, using using statistics derived from the
375 whole dataset statistics and by comparing individual picks at a given location along the fault.
376 Dataset statistics involve statistically comparing population means or medians to determine
377 their equivalence, with our approach outlined in Supplementary 7. To compare datasets
378 based for a specific uncertainty element (e.g., obliquity, cut-off type), we report the average
379 difference between population means, the average percentage (%) difference, and the
380 proportion of datasets that can be considered equivalent. Aggregated dataset statistics
381 allow for a direct comparison of properties across faults that have different lengths, and
382 therefore a different number of cut-off picks. Initially, we combine and discuss the obliquity
383 and repeatability statistics for each fault property (i.e., take the average values for absolute
384 difference, % difference, and % of equal datasets of the discontinuous and continuous
385 datasets). Subsequently, we compare discontinuous and continuous fault cut-off data,
386 transect obliquity and interpretation repeatability datasets in the same manner (see
387 Supplementary 7, for the full analysis).

388 **4 Results and the impact of uncertainties on fault properties**

389 We initially discuss the effect of our three investigated uncertainty elements (discontinuous
390 and continuous fault cut-offs, transect obliquity and interpretation repeatability) for
391 datasets containing data from all extracted fault properties (Section 4.1), before considering
392 their impact on individual properties (i.e., throw, heave, displacement, dip) (Sections 4.2 to
393 4.4).

394 ***4.1 All fault properties***

395 *Repeatability:* Of the repeatability datasets, only 46% (283 out of 616) were statistically
 396 equivalent, with an average difference in population mean/median of 16% (Table S1). The
 397 percentage of equivalent datasets varied between faults, ranging from 31% (SF1) to 56%
 398 (SF2), and the difference in population means ranged from 9% (SF2) to 28% (SF1). Repeat
 399 picks showed more uncertainty for horizon H9 (32% equivalent datasets, 20% difference)
 400 compared to H12 (59% equivalent datasets, 13% difference). This trend was consistent
 401 across all faults, although the magnitude of difference varied between faults. Overall, less
 402 than half of the repeat horizons could be considered equivalent.

Obliquity	a) % of oblique datasets that are statistically equal to the fault perpendicular dataset					Colour scale	b) % error between oblique and fault perpendicular datasets					Colour scale
	SF1	SF2	SF3	SF4	All faults		SF1	SF2	SF3	SF4	All faults	
-50	20%	28%	29%	54%	34%		65%	28%	38%	35%	38%	
-40	45%	19%	38%	64%	40%		26%	26%	26%	22%	25%	
-30	61%	38%	45%	83%	54%		17%	15%	17%	15%	16%	
-20	73%	72%	74%	88%	77%		13%	10%	8%	12%	10%	
-10	80%	84%	91%	95%	89%		16%	6%	4%	9%	7%	
10	73%	58%	66%	86%	70%		13%	10%	10%	11%	11%	
20	61%	88%	56%	85%	73%		19%	6%	12%	14%	12%	
30	39%	38%	42%	88%	52%		5%	15%	16%	18%	19%	
40	57%	30%	31%	58%	41%		21%	22%	25%	29%	25%	
50	30%	23%	22%	64%	34%		43%	41%	42%	25%	38%	
Total	54%	48%	49%	76%	56%		27%	18%	20%	19%	20%	

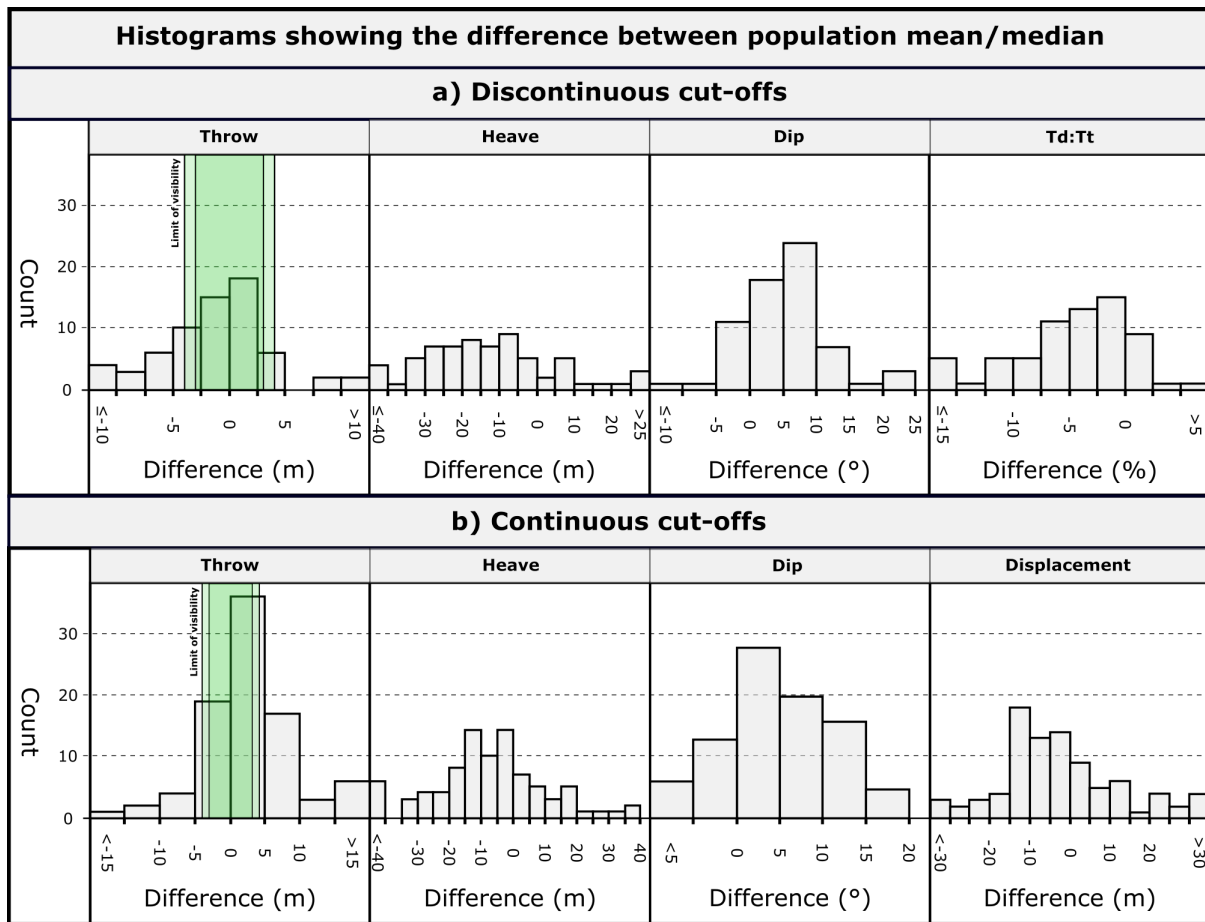
403
 404 **Figure 6: The effect of obliquity on extracted fault properties: a) the % of datasets for that fault and**
 405 **obliquity that are statistically equal to the dataset extracted for that horizon using an strike-perpendicular**
 406 **transect; b) the percentage error of all fault properties split by fault and obliquity. Colour scales differ**
 407 **between individual faults and all fault datasets so that red represents datasets that are highly affected by**
 408 **obliquity, and blue represents datasets where obliquity has a limited effect on extracted fault properties.**
 409 **Note how most values are blue (smaller errors) where obliquity is $\leq \pm 20^\circ$, suggesting that oblique sampling**
 410 **above this value should be avoided to minimise obliquity related errors.**

411 *Obliquity:* Greater errors were observed where the degrees of obliquity exceeded 20° (Fig.
 412 6). The same overall pattern was observed for individual faults, although there was more
 413 scatter in the data (Fig. 6). The percentage difference for any given obliquity also varied for

414 each fault. Some horizons are more prone to obliquity related errors (Table S2), suggesting
415 that horizon properties contribute to interpretation errors. For example, H9 which has
416 stronger reflectivity (Fig. 2a) displays lower percentage differences when compared to H1,
417 where reflectivity is weaker (Fig 2a, Table S2). Nevertheless, all horizons exhibited the same
418 general trend of increased uncertainty with increasing obliquity.

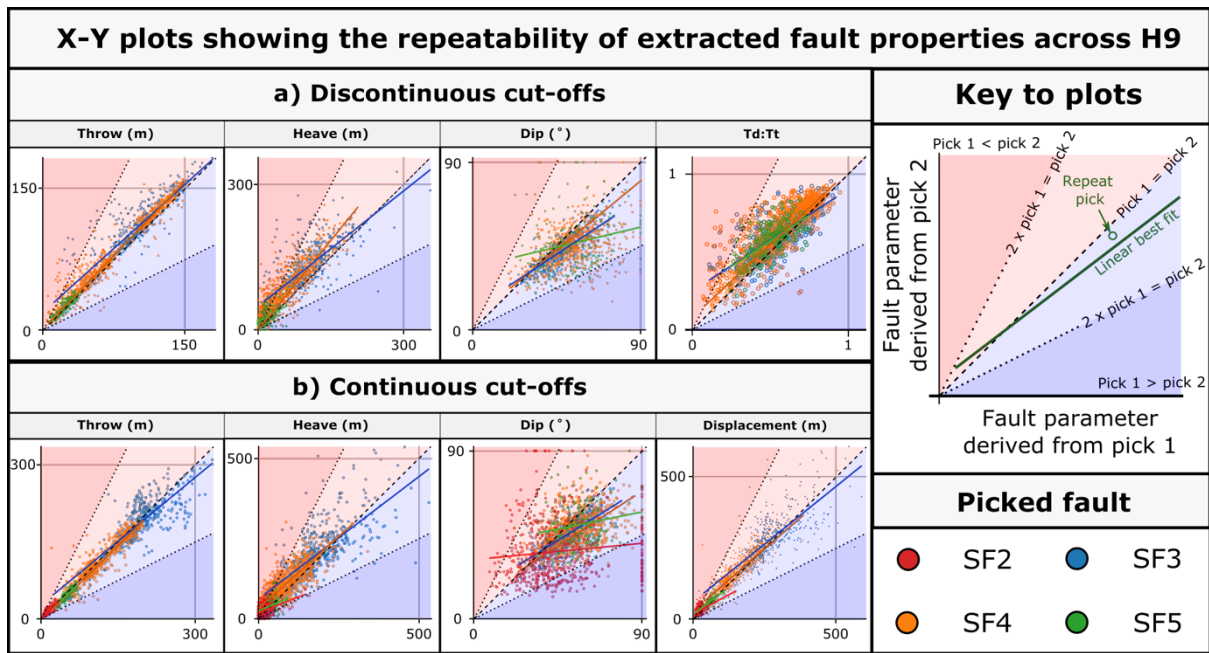
419 *Interpreted cut-off type:* The effect of cut-off type differed between obliquity and
420 repeatability datasets. For repeat interpretations, little difference was observed in the
421 uncertainty between continuous and discontinuous cut-offs, with 48% and 44% of datasets
422 considered equal. Conversely, the obliquity datasets displayed greater uncertainty for
423 continuous cut-offs (51% equal datasets) when compared to discontinuous cut-offs (63%
424 equal datasets) (Table S2). Certain horizons showed greater uncertainty in data extracted
425 from continuous cut-offs (e.g., H13 and H14); however, this was not always the case with
426 uncertainty being high (e.g., H1, H3, H11) or low (e.g., H9, H13) for both cut-off types for a
427 given horizon (Table S2). This suggests the interpreted cut-off type has a moderate effect on
428 obliquity datasets and a minor to negligible effect on repeat picks, with the horizon from
429 which the data is extracted being a key controlling factor on the magnitude of uncertainty.

430 Overall, when considering all fault properties: the interpreted cut-off type, the magnitude of
431 obliquity, and the fault and horizon from which the data is extracted, are identified as key
432 factors controlling interpretational uncertainty. To assess the effect of obliquity on
433 repeatability, it is important to separately considered the influence of uncertainty factors on
434 each fault property separately. This approach allows for the isolation of factors and the
435 comparison of obliquity errors to the theoretical errors introduced in Figure 3.



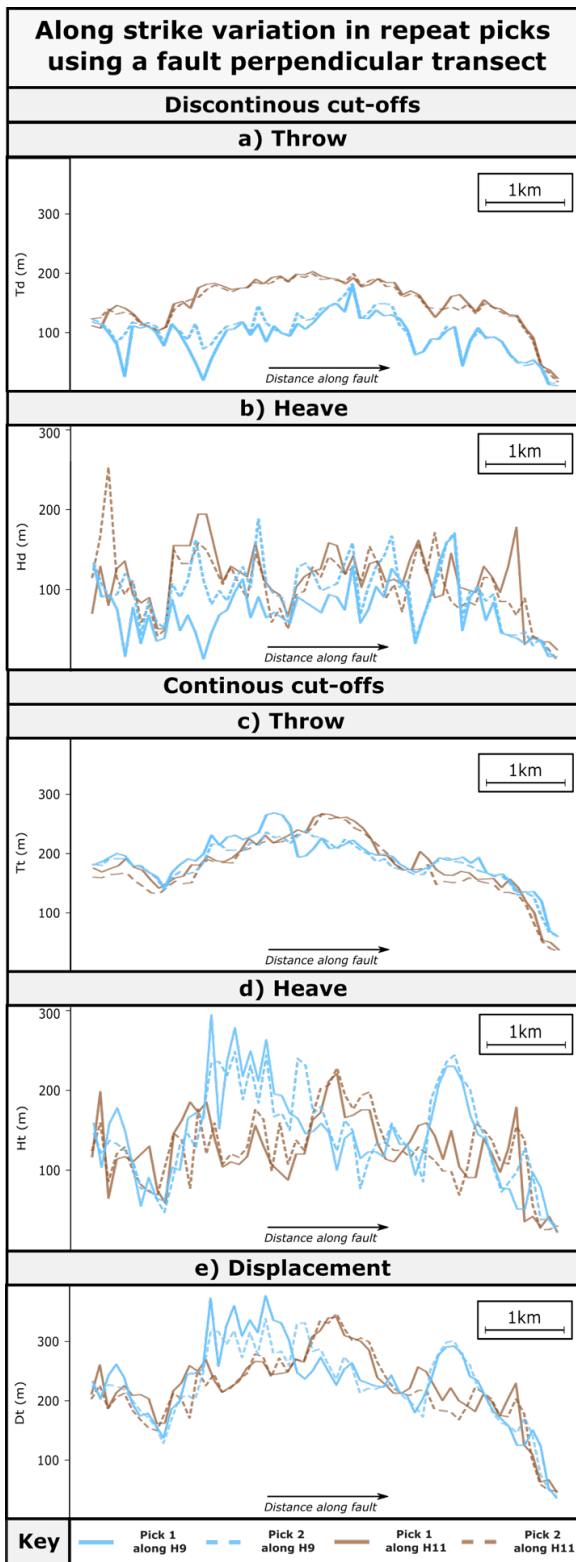
437

438 **Figure 7: Histograms to summarise the mean/median difference in fault properties extracted from**
 439 **discontinuous (a) and continuous (b) cut-offs between repeat picks at identical points, across a series of**
 440 **horizons and faults. Each ‘count’ represents a population mean or median for all data points collected for a**
 441 **single horizon across a single fault. The green box on the throw histograms highlights the minimum and**
 442 **maximum limit of visibility for the seismic cube. Differences within this box can be considered as below the**
 443 **resolution limit, and therefore not caused by repeatability errors. Note that for all extracted properties,**
 444 **continuous measurements show lower repeatability than discontinuous measurements.**



445

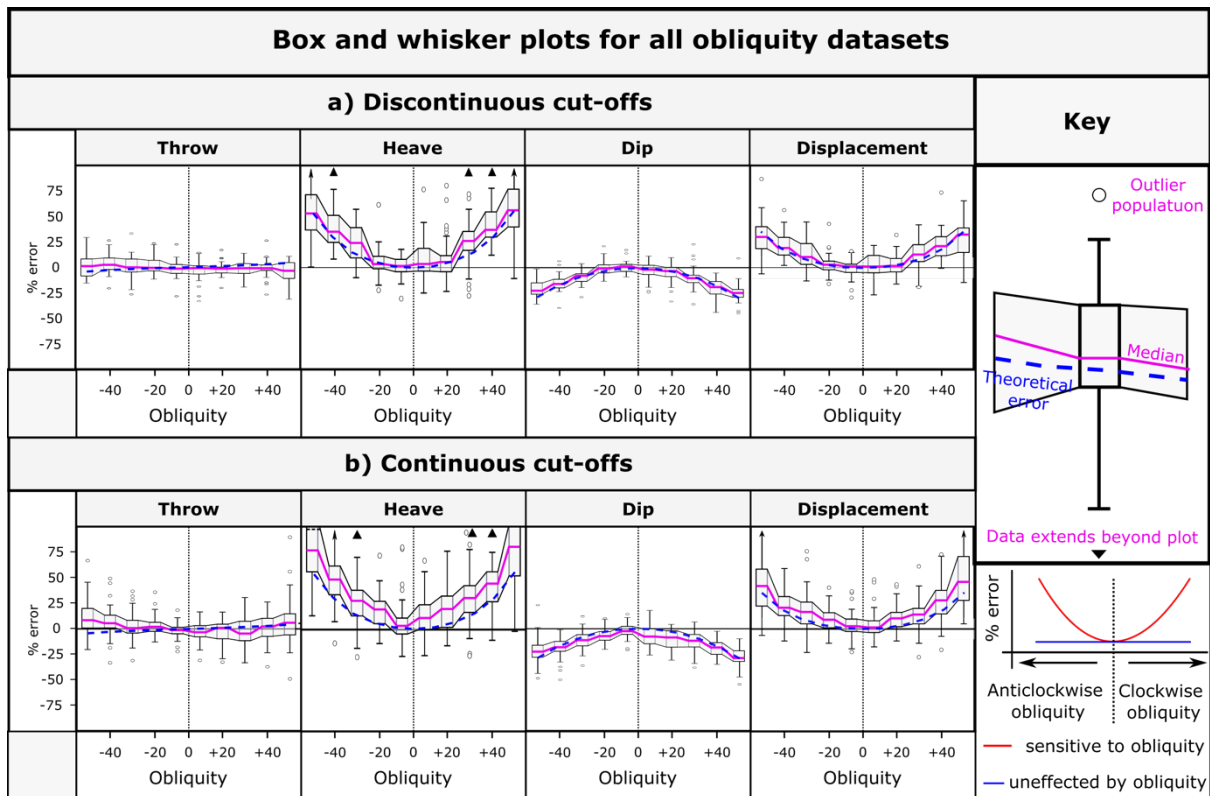
446 **Figure 8: x-y plots showing the variations in repeatability in discontinuous (a) and continuous (b) fault**
 447 **properties extracted from horizon H9 across all faults. If the interpretation is repeatable, then all points**
 448 **should plot along the black dashed x-y line; however, where picks differ the points will plot within the red or**
 449 **blue zone depending on the ratio of pick values. Data plotting in the darker red or blue zones represent data**
 450 **where one pick is over double the other. Note how the difference between picks varies between faults,**
 451 **extracted property, and the magnitude of the extracted property. Additionally, throw shows less**
 452 **repeatability error than heave.**



453

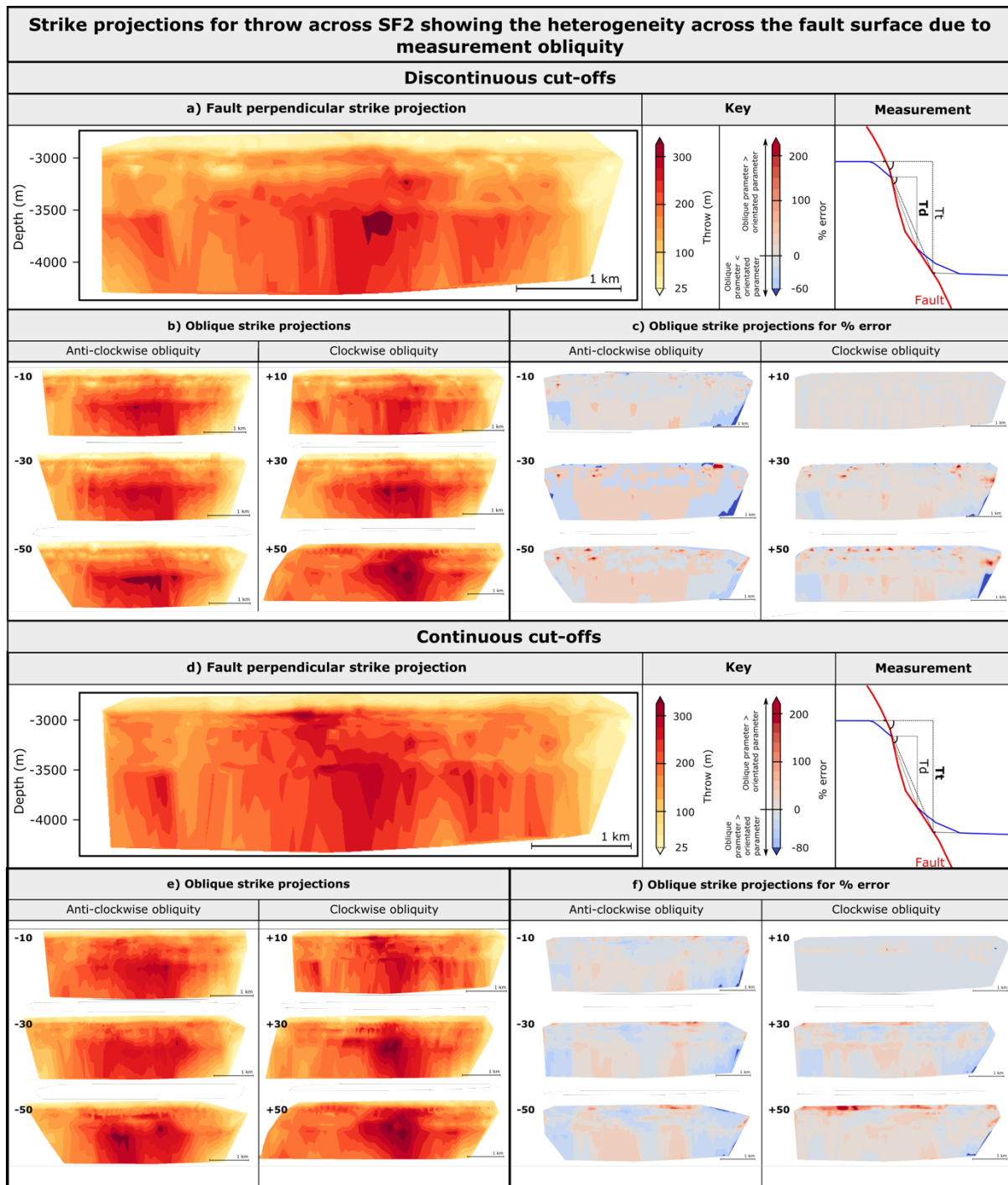
454 **Figure 9: Along-strike profiles showing the repeatability of fault property extracted from H9 and H12 using a**
 455 **strike-perpendicular transect along SF2. Pick one is shown as a solid line, whilst pick two is dashed and each**
 456 **horizon is a different colour. Note how the general shape of the profiles are similar between picks; however,**
 457 **the difference can be locally quite large.**

458 *Repeatability:* Throw exhibits low uncertainty across all repeatability datasets (Table S1, Fig
459 7, 8), with 60% of datasets considered equivalent, and there being only small differences in
460 means (5m, 7.4%). The mean absolute difference differs between faults, with differences
461 across all faults typically below the estimated seperability limit of the seismic data (Table
462 S1). Whereas differences in population means are minimal, this was not the case for all
463 picks along the fault. For example, Figure 9a and 9c show multiple locations where the
464 difference between picks on throw profiles extracted from discontinuous and continuous
465 cut-offs exceeds 22 m. The profiles also highlight sections of the fault with high and low
466 differences between picks, and that the location of these sections are not consistent
467 between horizons (i.e., H9 may show high variability at a particular along-strike location
468 where H12 shows low variability, and vice versa). This suggests that whereas horizons have
469 a limited effect on population statistics, they do influence individual picks. Overall,
470 repeatability errors primarily affect throw at a local scale (e.g., <500 m along strike distance)
471 and have a negligible effect on population statistics.



472

473 **Figure 10: The effect of obliquity on individual fault properties extracted from discontinuous (a) and**
 474 **continuous (b) cut-offs. Box and whisker plots are constructed from the population mean/medians of**
 475 **individual horizons picked across individual faults. Note how obliquity has the greatest effect on heave, and**
 476 **therefore dip and displacement, suggesting that additional care needs to be taken when sampling fault cut-**
 477 **offs for these properties. Furthermore, the median % error for all datasets typically exceeds the theoretical**
 478 **value for continuous cut-offs, suggesting some of the error is caused by non-geometrical effects.**



479

480

481

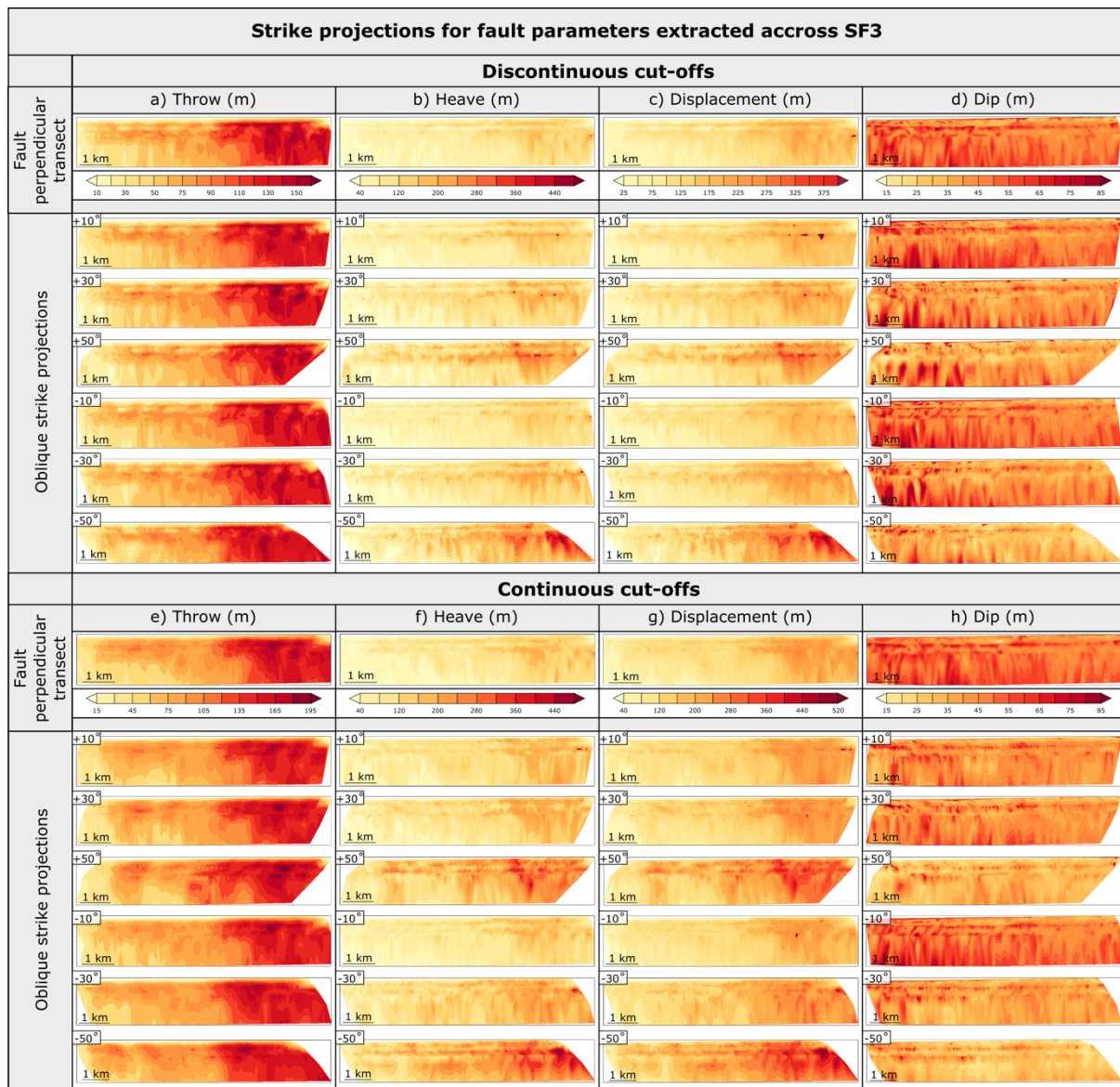
482

483

484

Figure 11: Strike projections showing the along-strike and down-dip variability caused by oblique sampling for throw extracted using discontinuous (a-c) and continuous (d-f) cut-offs along SF2. Data extracted from strike-perpendicular (a & d) and oblique (b & e) transects are shown, along with the % error associated with the oblique measurement (c & f). Note how the distribution and % error of throw depends on both the direction and magnitude of measurement obliquity. Strike projections are created using a python script that

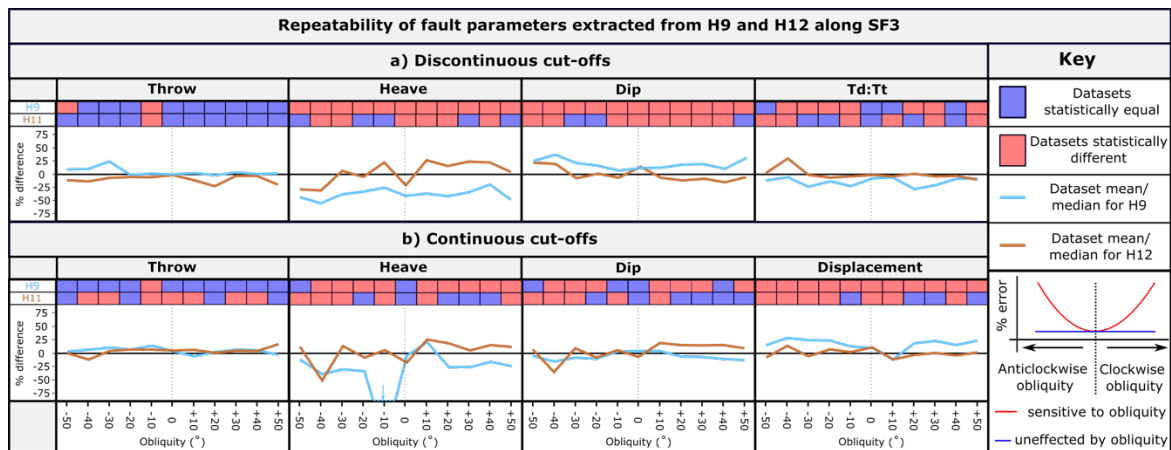
485 undertakes a linear interpretation between known datapoints, resampled to a regular sample spacing to
 486 enable the % difference between datasets to be calculated.



487
 488 **Figure 12: Strike projections showing the along strike and down dip variability of all studied fault properties**
 489 **calculated from discontinuous (a-d) and continuous (e-h) cut-off data extracted from SF3. Note how throw**
 490 **is less sensitive to measurement obliquity than heave and displacement and that dip shows high spatial**
 491 **variability across all datasets.**

492 *Obliquity:* Overall, throw typically displays increasing uncertainty as the obliquity increases
 493 (Table S2, Fig. 10); however, the error across the range of obliquity is low. Where individual

494 faults are considered, not all faults show greatest error at high degrees of obliquity (e.g.,
 495 SF1, SF4; Table S3). The picked horizon also has a large impact on the % difference for
 496 throw, although the overall trends of increasing uncertainty with increasing angles of
 497 obliquity are still observed. The distribution of throw across the fault plane varies at
 498 different degrees of obliquity (Figure 11, 12a, 12e) and can be over- or under- estimated at
 499 different locations, with % errors locally exceeding 100%. We suggest that changes in
 500 imaged horizon properties (e.g., acoustic impedance, amplitude of the reflection) influence
 501 the picked cut-off data and hence throw measurements. Obliquity errors exceed the
 502 theoretical geometrical errors (Figure 3) for throw for faults by $\pm 5\%$, with some horizons
 503 exceeding the expected error by a factor of 5 (Figure 10). The repeatability of throw does
 504 not appear to be sensitive to the degrees of obliquity as highlighted by: i) the distribution of
 505 statistically equal datasets and ii) given angle of obliquity can show both high and low %
 506 differences for the same cut-off type and horizon (Figure 13).



507
 508 **Figure 13: Repeatability of fault picks for fault parameters extracted using discontinuous (a) and continuous**
 509 **(b) cut-offs along horizons H9 and H12 for SF3. The plots show whether pick one and pick two can be**
 510 **considered equal, and the mean % difference between each pick. Note how there is no correlation between**
 511 **obliquity and repeatability error, suggesting that obliquity and repeatability are independent sources of**
 512 **error for this dataset.**

513 *Interpreted cut-off type:* The interpreted cut-off type affects the magnitude of repeatability
514 and obliquity errors. Average repeatability errors for throw are marginally higher for
515 continuous cut-offs (6.0 m, 9%) compared to discontinuous cut-offs (4.0 m, 5%) (Table S1).
516 In most cases, H9 showed greater errors compared to H12 for both cut-off types, with the
517 only exception being continuous cut-offs extracted from SF2 (Table S1). The magnitude and
518 location of along-strike variations between individual picks differed between horizons and
519 cut-off type (Fig 9). Indeed, there are examples where throw calculated from the first
520 discontinuous cut-off pick exceeds the second, with the opposite being true for continuous
521 cut-offs. For oblique transects, a far greater proportion of datasets are equal (91%), with a
522 lower % error (7%) for discontinuous cut-offs when compared to continuous cut-offs (75%,
523 11%; Table S7, S8). The magnitude of error increases for low-throw faults where the same
524 horizons show large and small error, albeit with continuous cut-offs showing greater errors.
525 The distribution of throw along- and down- dip is highly variable at different degrees of
526 obliquity (Fig 11, 12a, 12e), with the distribution and magnitude of throw depending on the
527 direction and degree of obliquity. Additionally, the patterns are not constant between
528 discontinuous and continuous cut-offs, as shown by the location of throw maxima in Figure
529 11 and 12a, e.

530 **4.3 Heave**

531 *Repeatability:* Heave shows high uncertainty across all repeat picks (Fig. 7, 8), with only 37%
532 of datasets considered equivalent and a reasonable difference between population
533 mean/median values (17.8 m, 27%). SF2 is less prone to repeatability errors when compared
534 to other faults (Fig. 8; Table S1). Repeatability errors are greater at lower values of heave, as
535 indicated by the higher % difference for SF1 and the x-y plots in Figure 8. Along-fault heave

536 profiles (Fig. 9b, d) show a large variability in the magnitude and difference between picks
537 for adjacent measurement positions (i.e., a large amount of noise in the data). Errors are not
538 consistent between horizons or measurement types and the difference between picks
539 locally exceeds 50 m (Fig 9b, d). This suggests that repeatability errors in fault and horizon
540 picks and how these vary along-strike effect the extraction of heave, creating uncertainty in
541 heave measurements.

542 *Obliquity:* The degree of obliquity has a large effect on heave, with uncertainty increasing
543 with increasing degrees of obliquity (Table S4). The mean absolute difference in heave
544 exceeds the average difference for repeat picks at obliquities of $\pm 30^\circ$ and shows a maximum
545 difference of 54.3 m (72%). This trend is observed across all faults; however, each fault
546 shows a different magnitude of error and proportion of equal datasets, with SF2 and SF3
547 appearing to be most prone to obliquity errors. When compared to theoretical geometric
548 errors (Figure 3, 10) most datasets show % errors that exceed the expected values by
549 between 5% and 10%, with the heave measurement for some horizons being particularly
550 prone to high errors. The effect of obliquity on the distribution of heave across the fault
551 plane depends on the fault and the direction and degree of obliquity (Figure 12b, f). For all
552 faults, the overall trend is that as obliquity increases, the proportion of positive % difference
553 also increases (irrespective of the absolute magnitude of heave). On top of these general
554 trends however there is a large amount of scatter in the data, which for some faults (e.g.,
555 SF1) lead to a high spatial variability in heave (Figure 12b, f). For all datasets, the angle and
556 direction of obliquity does not appear to affect the % difference between picks (Fig 13).
557 Overall, the degree of obliquity greatly affects the measurement of heave, with the error
558 compounded by large differences between along-strike sample locations.

559 *Interpreted cut-off type:* The interpreted cut-off type has a large effect on obliquity
560 statistics, although the effect on repeatability depends on the fault which the data are
561 extracted from (Table S1, Figure 13). For repeat picks, heave extracted from continuous cut-
562 offs shows a smaller difference in population mean (16.5m, 26%) and a higher proportion of
563 equivalent datasets (41%) compared to discontinuous cut-offs (19.0 m, 33% and 28%
564 respectively). However, this is not the case for SF2 where the opposite is true. Both cut-off
565 types show large along-strike variability; however, continuous cut-offs show less difference
566 between adjacent sample locations than discontinuous cut-offs (Figure 6). The
567 measurement of continuous cut-offs greatly increase the % error in obliquity statistics, with
568 the error nearly always greater than discontinuous cut-off data and the theoretical
569 geometrical error (Figure 1c, 7). Smoother profiles observed in the repeatability datasets are
570 mirrored where heave is calculated from continuous cut-offs, with these strike projections
571 appearing less noisy than the discontinuous cut-offs (Figure 12b, f).

572 **4.4 Displacement**

573 *Repeatability:* Displacement shows moderate uncertainty across all repeat picks (Table S1,
574 Figures 7, 8) with 47% of datasets considered equivalent and an absolute difference of 15.3
575 m (16%). The level of uncertainty differed between faults, with SF1 displaying the lowest
576 number of equivalent datasets (27%) and greatest % error (31%). The along-strike
577 displacement profiles (Figure 9e) show the same along-strike variability observed in the
578 heave profile, but with a lower magnitude of variability caused by the low variation in
579 throw. Sections of faults that show high, or low, differences between picks are more
580 laterally extensive (up to 1.5 km) than heave and match more closely the differences
581 observed in throw (Figure 9e).

582 *Obliquity*: Displacement exhibits increasing uncertainty at higher degrees of obliquity,
583 surpassing repeatability errors at $\pm 30^\circ$ (Table S5). The pattern observed in heave strongly
584 impacts the population statistics, with SF2 and SF3 showing the lowest proportion of
585 consistent datasets. Displacement varies across fault planes, with increasing magnitude at
586 higher obliquities (Figures 10, 12c, g). Like the heave datasets, the base syn-rift (H9) displays
587 a pronounced displacement maxima and significant variability between along-strike data
588 points (Figure 12c, g). Measurement obliquity does not systematically effect the
589 repeatability of fault displacement (Figure 13). Overall, displacement is more susceptible to
590 degree of obliquity than throw, with uncertainty in heave influencing the magnitude of
591 displacement and how this varies along the length of the fault.

592 *Interpreted cut-off type*: Interpreted cut-off type impacts repeatability and obliquity errors
593 differently (Table S1, Figure 8, 10). Displacement calculated from discontinuous cut-offs
594 exhibits greater differences between picks, and a lower proportion of equivalent datasets
595 compared to continuous cut-offs (Table S1). Both cut-off types show increasing uncertainty
596 with increasing degrees of obliquity; however, the magnitude of difference is greatest for
597 continuous cut-offs (Figure 10). However, for some faults, highly oblique continuous cut-off
598 datasets may exhibit low uncertainty (e.g., SF4, Table S12) and the displacement strike
599 projections constructed for continuous cut-offs are smoother than discontinuous cut-offs
600 (Figure 12c, g). Despite this, repeatability errors are usually exceeded where measurement
601 obliquity is at or above $\pm 30^\circ$. Overall, interpreting continuous cut-offs reduces the
602 repeatability of displacement on some horizons and measurement obliquity greatly affects
603 continuous datasets .

604 **4.5 Dip**

605 *Repeatability:* Of all the fault properties, dip exhibits the highest uncertainty in repeat picks
606 (Figure 7, 8, Table S1), with only 32% of datasets considered equivalent and an absolute
607 difference of 6.6° (16%). The fault from which the data is extracted influences the
608 magnitude of uncertainty in dip, with SF1 showing a mean absolute difference of 9.2° ,
609 whereas SF2 only has a difference of 3.2° . Unlike heave and displacement, the magnitude of
610 dip appears to only have a weak effect on repeatability (Figure 8). Individual picks on SF1
611 show very large differences, with several picks having a dip of 90° (indicating zero heave),
612 whereas the paired pick ranges from $\sim 15^\circ$ to $\sim 65^\circ$ (Fig 8). These picks are taken from where
613 there are very small offsets along SF1, thus heave is likely below the resolution of the data
614 here (minimum heave values of ~ 6 m). Due to the compound errors caused by the
615 uncertainty in heave, dip shows low repeatability and along-strike variations can be masked
616 by measurement errors.

617 *Obliquity:* Fault dip is strongly affected by measurement obliquity, with repeatability errors
618 exceeded for most oblique datasets (Figure 10, Tables S1, S5). In a similar manner to
619 displacement, the effect of uncertainties on heave strongly affects the calculation of dip
620 (i.e., SF2 and SF3 showing the lowest % of equal datasets), although greater uncertainty is
621 observed for the latter (Table S5). Repeatability errors are exceeded where the angle of
622 obliquity exceeds $\pm 20^\circ$ for all faults, apart from SF1 where repeatability errors were
623 particularly high (Table S5). The distribution of dip across the fault plane displays a high
624 degree of variability between points leading to noisy strike-projections (Figure 12d, h).
625 Despite this, general trends are observed across all obliquities (e.g., shallower dips at the
626 syn-rift horizon (H9)); however, the magnitude of dip is lower at higher degrees of obliquity.

627 In most cases, there is no correlation between the degree of obliquity and repeatability
628 (Figure 13).

629 *Interpreted cut-off type:* The choice of cut-off type affects repeatability and obliquity
630 datasets differently. Across all faults, the choice of cut-off type does not affect the
631 repeatability of dip, with similar differences and percentage of equal datasets observed.
632 Whether discontinuous or continuous cut-offs, uncertainty depends on the fault and
633 horizon the data is collected from, with H9 broadly showing greater uncertainty than H12
634 (ref a figure or table). When individual cut-off picks are considered, there is more scatter in
635 the continuous cut-off data, than the discontinuous, (Figure 8), with many picks exceeding
636 100% difference. Despite this, profiles constructed from continuous cut-offs show less
637 along-strike variability (Figure 9). Measurement obliquity affects both cut-off types;
638 however, the effect is greater for continuous cut-offs (Table S13, S14). This trend is
639 observed across all faults, however, the magnitude of error and difference between cut-off
640 types depends on the fault and the horizon that the data are extracted from. It is difficult to
641 assess the effect of cut-off type on the distribution of dip across the fault plane as both
642 exhibit a highly variable distribution of dip for all datasets (Figure 12d, h). Overall, no
643 systematic difference between cut-off type is observed for dip repeatability, and whereas
644 the measurement of continuous cut-offs increases errors associated with obliquity, datasets
645 are very noisy and it is not possible to deduce along-fault trends.

646 **4.6 Summary of results**

647 Our data show that fault properties extracted from fault-horizon cut-offs are variably
648 influenced by interpretation repeatability, measurement obliquity, and the measured cut-

649 off type (Table 1). When all properties were considered together, less than half of the
650 datasets could be considered statistically equal. Errors due to measurement obliquity were
651 found to greatly increase when obliquity exceeded $\pm 20^\circ$. Measurements of continuous cut-
652 offs showed greater errors than discontinuous cut-offs in both the obliquity and
653 repeatability datasets. The magnitude of error was also influenced by which fault and
654 horizon the data were collected from.

655 When individual fault properties are considered, throw is found to be the least sensitive
656 fault property to the studied interpretation factors, and heave the most sensitive (Table 1).
657 Uncertainties in throw increased when measurement obliquity exceeded $\pm 20^\circ$; however, the
658 magnitude of uncertainty was often below or close to the limit of separability of the seismic
659 cube (i.e., not a significant source of error) apart from at a local (<500 m) scale. Heave was
660 found to show statistically significant differences for both repeat and oblique datasets.
661 Differences were particularly evident at a local scale and caused strike projections and
662 along-strike profiles to be noisy. The fault and horizon cut-off that the data were extracted
663 from had a subsidiary effect on extracted fault properties (e.g., heave and throw), with the
664 magnitude of obliquity not compounding repeatability errors. Across most fault properties,
665 continuous cut-off picks were more susceptible to repeatability and obliquity errors. Despite
666 showing greater uncertainty for continuous picks, continuous datasets show less along-
667 strike variability between adjacent picks, leading to smoother along-fault profiles and strike
668 projections. The ratio of throw extracted from discontinuous to continuous cut-offs
669 indicates that the errors from the continuous and discontinuous datasets were compounded
670 where the properties were compared, and the noisiness of the discontinuous profiles lead
671 to large variations in the ratio between discontinuous and continuous throw between

672 adjacent picks across a fault. Uncertainty in heave also increases uncertainty in
 673 displacement and dip (as these properties are geometrically derived using heave), with the
 674 effect particularly noticeable in along-fault profiles and strike projections. For dip, it was
 675 found that this local scale uncertainty often masked overall trends in dip and caused profiles
 676 and strike projections to be very noisy (Figure 12d, h).

677 In the following section, we investigate how our results on uncertainties in cut-off derived
 678 fault properties affect the assessment of fault transmissivity and the evolution of throw- and
 679 slip-rate through time. We make this investigation to demonstrate the potential impact of
 680 interpretation choices and repeatability on fault properties used in the prediction of crustal
 681 fluid-flow and in the assessment of seismic hazards.

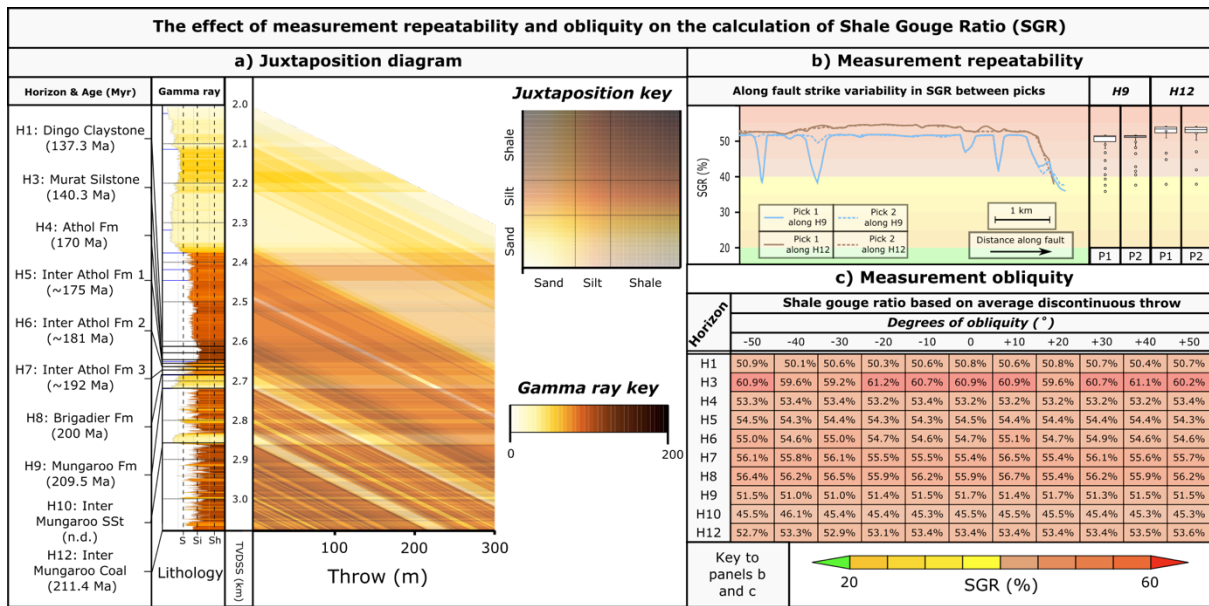
Fault property	Repeatability	Measurement obliquity	Interpreted cut-off type
All fault properties	Repeat datasets are often not equivalent, with the % difference depending on the fault and horizon that the data is extracted from.	Error is found to increase where obliquity exceeds $\pm 20^\circ$. The fault and horizon that the data is collected from also has a subsidiary effect.	Greater uncertainty in continuous cut-offs compared to discontinuous; however, the difference is low to moderate for obliquity datasets and negligible for repeat picks.
Throw	High repeatability Errors only significant at a local scale (i.e., <500 m).	Moderate sensitivity Errors increase as obliquity increases and are larger than predicted. Overall differences in population means are generally small.	High sensitivity Uncertainty increases in faults with low throw. Throw distribution is variable and influenced by the horizon and measurement obliquity.
Heave	Low repeatability Depends on the fault, horizon, and along-strike position that the data is collected from.	High sensitivity Errors are compounded due to differences between along-strike sample locations.	High sensitivity Continuous cut-off data exhibits smoother along-strike profiles but with increased errors at high obliquities.
Displacement	Moderate repeatability Along-strike patches of low repeatability more closely match the shape of the throw profile.	High sensitivity Due to high uncertainty in heave influencing the distribution and magnitude of displacement.	Moderate sensitivity Measurement obliquity greatly effects continuous cut-off datasets, whilst also causing strike projections to be smooth.
Dip	Low repeatability Along-strike variations are often obscured by measurement errors	High sensitivity Overall dip increases with obliquity, and there are large spatial variations across the fault plane.	Low sensitivity Datasets are very noisy and it is not possible to deduce along-fault trends.

682 **Table 1: Summary of the effects of interpretation uncertainty on the extracted fault properties. Note how**
683 **heave is more prone to interpretational uncertainty than throw, which also affects the extracted dip and**
684 **displacement.**

685 **5 Effect of obliquity and repeatability uncertainty on inferred fault properties**

686 Data extracted from 3D seismic reflection surveys are used across a range of scientific
687 studies, and therefore the sources of uncertainty presented in this paper have implications
688 for the geological analyses that arise. Drawing on data from the interpretation of SF2, we
689 discuss the implications for two such analyses, fault transmissivity which is important for
690 quantifying fluid flow, and slip/throw rates used to inform seismic hazard assessment.
691 Throw extracted from discontinuous cut-offs is used for fault transmissivity and throw-rate
692 calculations, whereas continuous cut-offs are used when assessing the evolution of slip-rate
693 to account for non-discrete deformation (e.g., monocline development). These examples
694 demonstrate the practical effect of the investigated uncertainty elements on fault property
695 predictions.

696 ***5.1 Fault transmissivity interpretation using discontinuous deformation***



697

698 **Figure 14: The effect of repeatability and obliquity on the estimation of shale gouge ratio for fault**
 699 **transmissivity studied. Note how for this fault all values are above the sealing threshold, and the effect of**
 700 **repeatability and obliquity related errors are only locally important.**

701 Cross-fault transmissivity describes the ability of fluid to flow across a fault zone. The
 702 potential for cross-fault flow is important to quantify for hydrocarbon production, CO₂
 703 sequestration and the geological disposal of nuclear waste. A common method used to
 704 assess fault transmissivity is to calculate the shale gouge ratio (SGR, e.g., Yielding et al.,
 705 2002), by considering the proportion of shale that has moved past a given point on a fault
 706 using the following equations:

707

$$V_{shale} = \frac{GR_z - GR_{min}}{GR_{max} - GR_{min}}$$

708

(V_{shale} = proportion of shale in a given rock volume, GR_z =

709

Gamma ray reading at a specific depth, GR_{min} =

710

minimum gamma ray reading, GR_{max} = maximum gamma ray reading)

711
$$SGR = \frac{\sum(V_{shale} \times \Delta z)}{throw}$$

712 ($\Delta z = bed\ thickness$)

713 A higher SGR ratio suggests that there is a high proportion of phyllosilicates (shale) within
714 the fault core (e.g., Foxford et al., 1998; Yielding, 2002). An SGR of 15-20% has been
715 suggested as a sealing limit (Yielding, 2002); however, it should be noted that this value is
716 based on relatively shallow reservoirs (<3 km) and that fault permeability may be orders of
717 magnitude lower or higher than reservoir properties (Bense et al., 2013). In this section we
718 investigate how the calculation of SGR is effected by differences in fault throw caused by
719 measurement obliquity and repeatability errors. Some software also enable fault
720 displacement to be used as an input. Whilst we do not explore how displacement influences
721 SGR in this section, the greater uncertainty caused by measurement obliquity, and lower
722 repeatability, of displacement suggests that greater uncertainty in SGR will arise when
723 displacement is used as an input. It should be noted that it is not our aim to characterise the
724 sealing potential of SF2, but instead highlight how our findings may effect the calculation of
725 SGR.

726 We manually calculate the SGR at each horizon-fault cut-off pair for the repeatability
727 datasets of throw across SF2. Due to the large number of horizons and datasets, we assess
728 how the differences in mean throw effect SGR for each horizon and degree of obliquity. The
729 purpose of using mean values is to demonstrate the impact of differences in throw caused
730 by measurement obliquity on the calculation of SGR. We use the Chandon-1 well, resampled

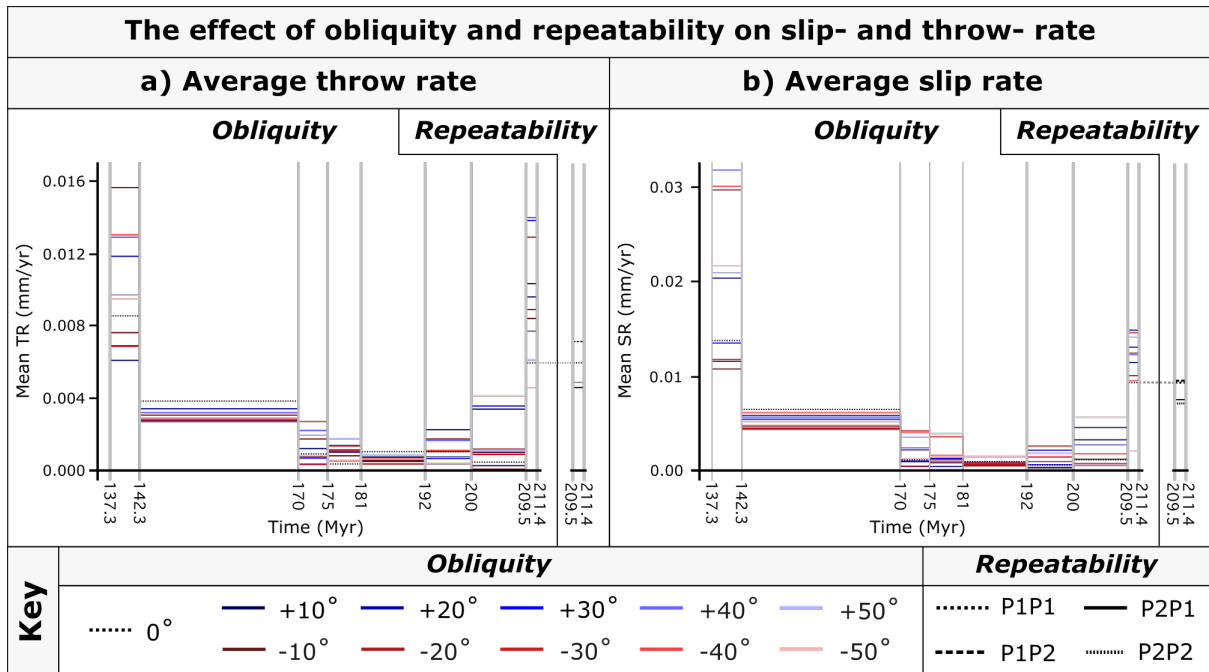
731 to every metre, to calculate V_{shale} of the succession and to construct juxtaposition diagrams
732 (Figure 14a).

733 Our assessment shows that repeatability and obliquity errors have only a minor impact on
734 the SGR calculation across SF2 (Figure 14b, c), with the V_{shale} of the intervening succession
735 playing a more significant role in the calculation. The interval of interest between H1 and
736 H12 is characterised by high V_{shale} values (average = 50%). As a result, most offsets exhibit
737 siltstone-shale or shale-shale juxtapositions (Figure 14a). Despite some differences between
738 repeat datasets, the mean values of SGR for H9 and H12 show negligible variations, with
739 larger differences observed only locally over short distances (<500 m). This is important for
740 assessing the juxtaposition windows of reservoir units, as the magnitude of these difference
741 could be sufficient to enable across fault fluid flow. It also suggests that the use of
742 population statistics are insufficient when assessing the location of leakage points using SGR
743 analysis.

744 Obliquity datasets also demonstrate variations in SGR between horizons, but the differences
745 between datasets for the same horizon are low (Figure 14c). The abundance of shale-shale
746 or sand-shale juxtapositions explain these low differences; however, it should be noted that
747 the magnitude of difference between picks would be similar in more sand rich successions.
748 This would cause SGR values to be more sensitive to uncertainties in throw as smaller
749 changes in throw could push the SGR above or below the sealing threshold. Similarly, to the
750 repeatability datasets, obliquity datasets likely show patches where changes in SGR
751 between datasets are high. Indeed, local changes in throw observed on Figure 9, 11, and 12
752 support this suggestion. It is beyond the scope of this study to explicitly explore the effect of
753 obliquity and repeatability on the transmissivity of reservoir bounding faults; however, our

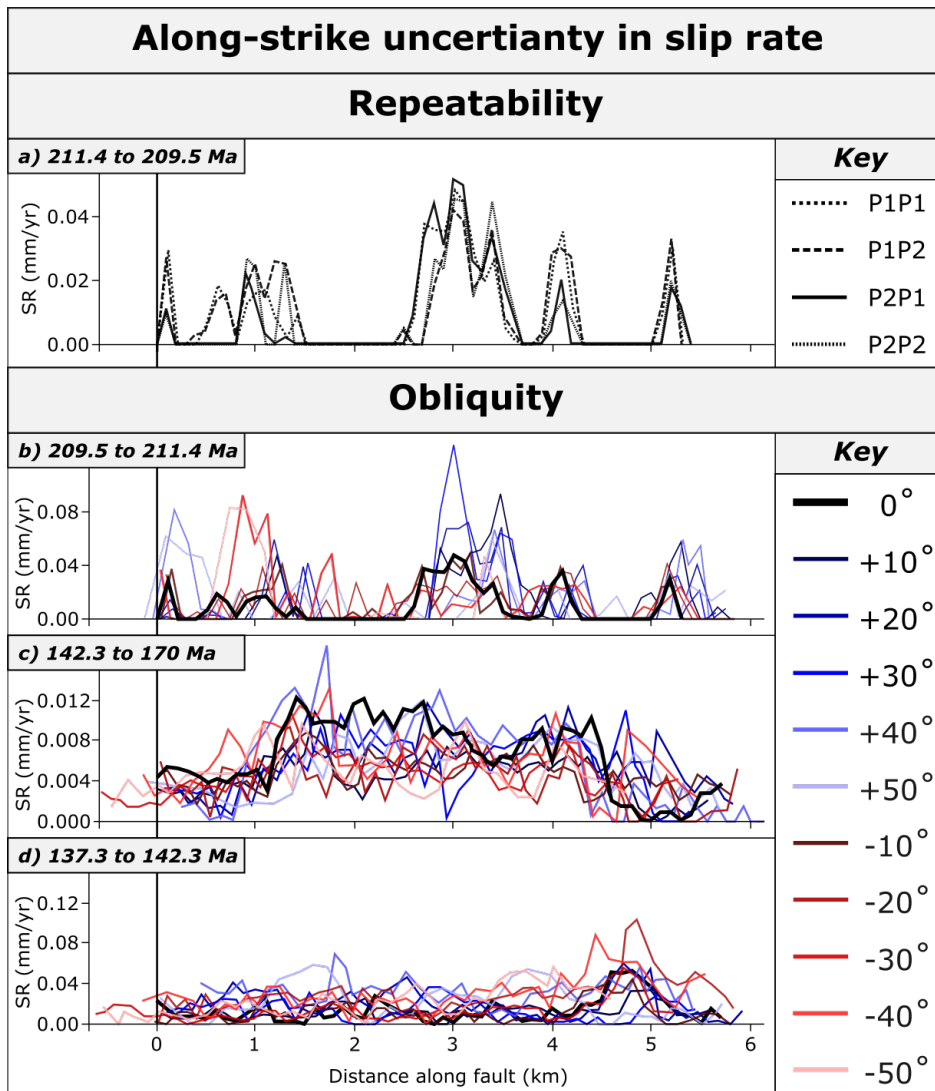
754 results suggest that repeatability and obliquity errors in throw could cause a difference in
 755 the location and sealing potential of juxtaposition windows.

756 **5.2 Throw and slip on faults over time using discontinuous and continuous deformation**



757

758 **Figure 15: The effect of repeatability and obliquity on the throw- and slip- rate of SF3 over time. Obliquity**
 759 **errors exceed repeatability errors for both mean throw- and slip-rate, and the effect of obliquity varies**
 760 **between time periods. P1 and P2 relates to the first and second pick across a given horizon, with the first**
 761 **value relating to H12 and the latter to H9. I.e., P1P2 relates to slip rate calculated using the 1st pick across**
 762 **H12 and the second pick across H9.**



763
 764 **Figure 16: The effect of repeatability and obliquity on the throw- and slip- rate evolution of SF3. Note how**
 765 **the shape of the profile differs between time periods, and between different measurement obliquities**
 766 **within that time period.**

767 When sediment accumulation rate exceeds fault throw rate, comparing the difference in
 768 throw or slip across two age-constrained horizons allows for the investigation of long-term
 769 throw or slip rate, which has applications for understanding fault growth (Marsh et al.,
 770 2010; Osagiede et al., 2014; Pan et al., 2022), strain partitioning between genetically related
 771 fault systems (Meyer et al., 2002; Cowie et al., 2005; Marsh et al., 2010) and using slip rates
 772 to understand and quantify seismic hazard (Nicol et al., 2005; Gambino et al., 2022).

773 In our study, we focus on the impact of measurement obliquity uncertainty on throw and
 774 slip rate across SF2 using multiple age-constrained horizons. Repeat picks were limited to
 775 Horizons H9 and H12, restricting our examination of the effect of repeatability on temporal
 776 slip-rate evolution, but enabling comparison of repeatability and obliquity errors for the
 777 211.4 to 209.5 Ma period (Figure 15). We calculate throw- and slip-rate using the
 778 continuous portion of the deformation, to account for any strain accommodated by near-
 779 fault deformation (e.g., monocline formation). We take the difference in throw between
 780 each horizon, and divide this by the time period between the two horizons using the
 781 following equations:

$$782 \quad \frac{throw_{H2} - throw_{H1}}{Age_{H2} - Age_{H1}}$$

$$783 \quad \frac{Displacement_{H2} - Displacement_{H1}}{Age_{H2} - Age_{H1}}$$

784 Where H1 is the shallower horizon, and H2 the deeper horizon across the time-period of
 785 interest. Whereas uncertainties exist in the age of horizons, we do not consider these
 786 uncertainties here as they affect each dataset equally. Additionally, using the same horizon
 787 for each obliquity pick eliminates uncertainty introduced by mapping different reflections of
 788 potentially different ages.

789 *Repeatability (211.4 to 209.5 Ma):* Uncertainty in throw and slip rate, obtained from repeat
 790 picks, is influenced by the picks used and along-strike variations in fault properties (Figure
 791 15, 16). Four pick combinations were analysed, resulting in mean throw rates ranging from
 792 0.0045 to 0.0071 mm/yr. The percentage difference of these values (-14% to 26%) exceed
 793 the repeatability of throw extracted from the continuous cut-off analysis. Mean slip rates
 794 ranged from 0.0071 to 0.0095 mm/yr. Unlike throw rates, no correlation was observed

795 between picks and mean slip rates, with the greatest difference occurring where horizon
796 picks from the same interpretation session were used. The difference in behaviour between
797 throw and slip rates indicates that whereas throw was consistently lower for pick 1 when
798 compared to pick 2, the same trend does not hold for heave. Along the fault, the slip rate
799 profile showed similar shapes for all pick combinations, but subtle differences were
800 observed, highlighting locations that were more susceptible to repeatability errors.
801 Therefore, in cases with low to modest difference in slip (average 11 m) between horizons,
802 the shape and magnitude of the slip profile may be influenced by repeatability errors.

803 *Obliquity:* The errors for throw and slip rates due to measurement obliquity exceed the
804 repeatability errors for datasets (Figures 15, 16). Measurement obliquity can affect the
805 estimates of mean throw and slip rates, as compared to data collected from a strike-
806 perpendicular transect (Figure 15). From 211.4 to 209.5 Ma, throw rates extracted from
807 oblique transects ranged from 0.0045 to 0.0140 mm/yr (absolute errors ranging from 3 to
808 135%), with only the -50° dataset having a lower throw rate than the strike-perpendicular
809 transect. For the same time period, mean slip rates range from 0.0095 and 0.0149 mm/yr
810 (absolute errors ranging from 1 to 60%), with all datasets (except -50°) exceeding the strike-
811 perpendicular transect. The effect of measurement obliquity varies through time and
812 differed between throw- and slip-rate (Figure 15). Oblique sampling resulted in over- or
813 under-estimations of throw and slip rates, with no consistent pattern observed. Along-fault
814 profiles were sensitive to both repeatability and obliquity errors, altering the location and
815 magnitude of throw- and slip-rate minima and maxima (Figure 16). The influence of
816 measurement obliquity on slip-rate profiles depended more on the time period measured
817 (i.e., which pair of horizons were sampled) than the magnitude of measurement obliquity.

818 Overall, even modest measurement obliquities (i.e., $\pm 20^\circ$), and to a lesser extent
819 repeatability errors, led to large differences in fault length inferred from along-fault profiles
820 and throw- or slip-rate used to calculate fault-based seismic hazard.

821 **6 Discussion**

822 ***6.1 Impact and mitigation of fault interpretation uncertainty***

823 ***Interpretation repeatability***

824 From our study, we conclude that where the quality of the seismic imagery is good and the
825 data are extracted by an interpreter with a similar level of experience, the repeatability of
826 extracted data will depend on the fault property being extracted, and the fault and horizon
827 that the data is extracted from (Table 1). Throw was found to be least sensitive to
828 repeatability errors (7%), with heave (27%), displacement (16%) and dip (16%) showing
829 greater sensitivity. Previous work has suggested that the interpretation of fault properties
830 from low-displacement dyke-induced faults could be affected by measurement
831 uncertainties of between $\pm 5\%$ (Magee and Jackson, 2020a) and $\pm 10\%$ (Magee et al., 2023).
832 Our study highlights that this range is not sufficient to capture the uncertainty in heave (and
833 therefore displacement and dip), particularly if multiple interpreters with greater subjective
834 bias are involved.

835 *Suggestions:* Repeatability errors are difficult to quantify and will depend on the quality of
836 the seismic image, the experience of the interpreter, and other human factors. As such the
837 appropriate size of the error bars will differ from the values presented in this study.

838 However, our study provides a first-pass parametric study of the influence of repeatability

839 errors on the extraction of fault properties, suggesting errors >10% are to be expected,
840 particularly in low-quality datasets or where low-displacement faults are present.
841 Additionally, studies that rely on displacement as an input will likely show greater
842 uncertainty compared to those that use throw as an input. Study specific error values could
843 be obtained by undertaking repeat picks on a subset of the data.

844 ***Measurement Obliquity***

845 From our study, we conclude that the derived measurement obliquity broadly follows the
846 theoretical trends (Figure 3), but that the magnitude of the resulting error exceeds the
847 theoretical values. The higher than expected errors may be due to 'non-geometrical'
848 obliquity errors of the type discussed in Section 6.2. Our findings suggest that measurement
849 obliquity should be limited, where possible, to $\pm 20^\circ$ around the orthogonal to the local fault
850 strike.

851 However, it may not be practical to always interpret orthogonal to the local fault strike, for
852 example when only 2D seismic datasets are available, or when the fault strike is highly
853 variable. For a fault that is highly sinuous, it would be time-consuming to construct
854 numerous arbitrary lines orthogonal to differently orientated fault sections. In that case,
855 additional steps would be required to ensure that the picks from differentially orientated
856 arbitrary lines are combined in a mathematically and geometrically appropriate way.

857 *Suggestions:* Measurement obliquity should not exceed $\pm 20^\circ$, and where possible $\pm 15^\circ$. This
858 ensures that obliquity errors are minimised, whilst still ensuring that data is collected in a
859 time-efficient manner. This rule is particularly important when continuous cut-offs are

860 measured. Where it is not possible to reduce the measurement obliquity, results could be
861 improved by 'correcting' heave, dip, and displacement values based on local strike
862 calculated from measured cut-offs and the theoretical relationships outlined in Figure 3.
863 However, whilst this would decrease the overall errors, it cannot account for any non-
864 geometrical errors in the dataset.

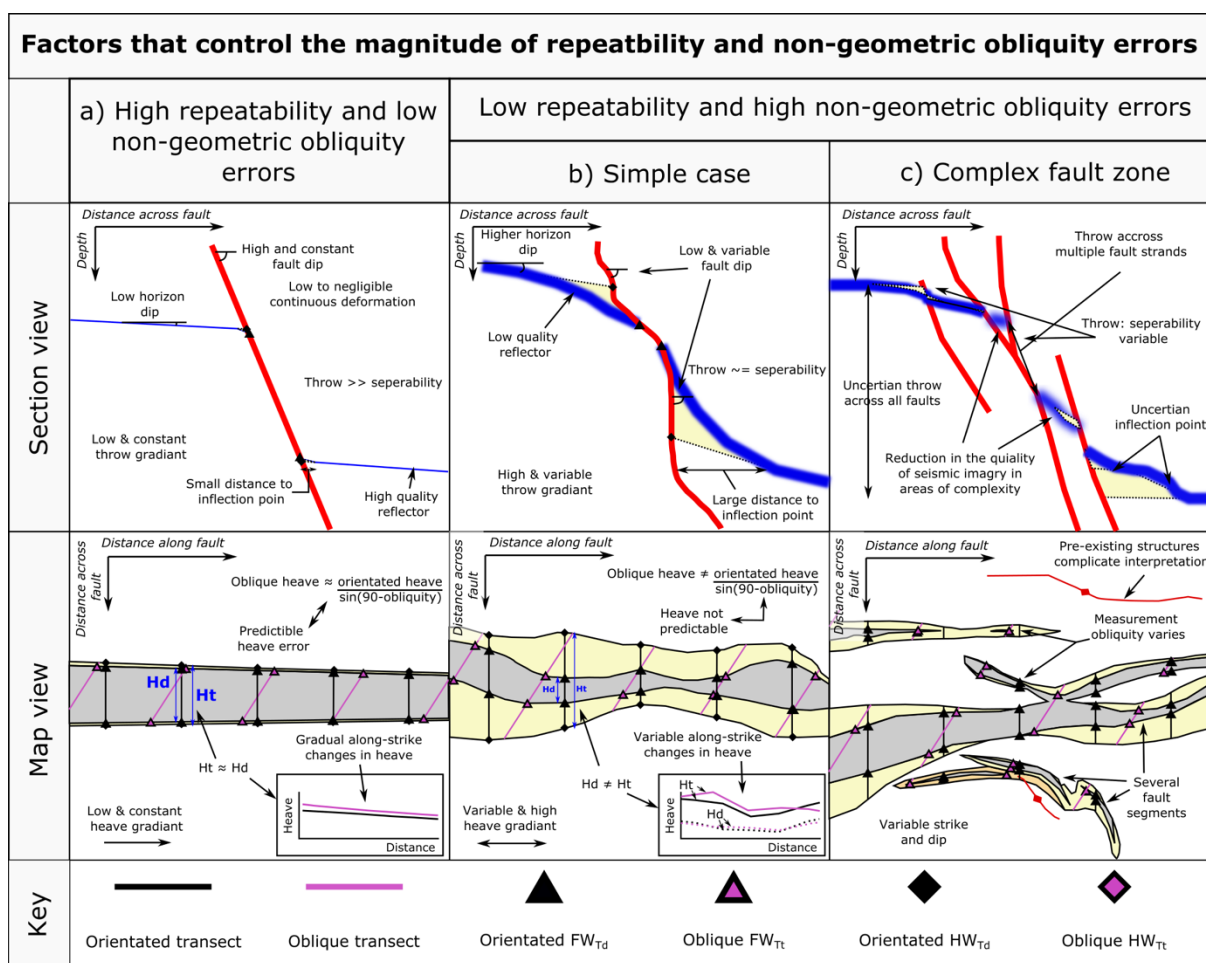
865 ***Interpreted cut-off type***

866 Our work highlights that the interpreted cut-off type influences the magnitude of both
867 repeatability and obliquity related errors (Tables 1, S7-14, Figures 7-13). Greater uncertainty
868 was observed where continuous cut-offs are included in the analysis, with the effect
869 particularly clear when extracting heave (Table 1, Figure 10).

870 *Suggestions:* The choice of interpreted cut-off type is often driven by study design. For
871 example, assessing fault transmissivity necessitates discontinuous cut-offs to account for
872 physical disconnections across the fault, while calculating long-term strain rate requires
873 continuous cut-offs to accommodate non-discrete deformation. However, we found that
874 the extraction of heave from fault cut-offs is particularly sensitive to both repeatability and
875 obliquity errors and that the magnitude of error for the latter can greatly exceed theoretical
876 values. Therefore, it may be better to use an average dip between two or more mapped
877 horizons to calculate heave from the measured throw value. This will also reduce the effect
878 of sample-specific measurement errors on the extraction of slip-rate.

879 ***6.2 Factors that control the magnitude of repeatability and non-geometrical obliquity*** 880 ***errors.***

881 Our study suggests that the extraction of fault properties from cut-off data is strongly
 882 affected by the three elements of fault interpretation focused on in this study, and that
 883 these elements contribute to uncertainty in deriving interpretations from these data.
 884 Additionally, the effect of each element can vary both between faults and spatially along a
 885 single fault. During the work, we identified several additional factors that combine to
 886 increase, or decrease, the uncertainty at a given point along the fault, which are
 887 summarised below and in Figure 17.



888
 889 **Figure 17: Cartoons showing the factors that control the repeatability and magnitude of non-geometric**
 890 **obliquity errors. Examples are shown for a fault with high repeatability and low geometric errors (a), low**
 891 **repeatability and high geometric errors (b), and a more complex fault zone that is representative of relay**
 892 **zones observed in the seismic cube. See text for discussion of these factors.**

893 Our data suggests that the quality of the mapped reflection plays a large role in non-
894 geometrical errors and low repeatability (Fig. 2a), as evidenced by certain horizons (e.g., H1)
895 showing high errors (Table S2). Our findings thus agreed with previous studies, in that the
896 quality of the seismic image, in particular the reflector strength, affects the reliability of the
897 interpretation derived from the image (e.g., Alcalde et al., 2017; Schaaf and Bond, 2019;
898 Chellingsworth et al., 2015). The effect of the reflection quality does not influence each fault
899 property equally, with heave (and thus displacement and dip) affected more than throw,
900 due to the low regional dip ($<3^\circ$) across the study area.

901 Our data shows that the uncertainty is affected by the size of the fault in terms of
902 displacement or throw. There is greater uncertainty in areas of low throw, especially when
903 close to or below the limit of separability. When a large proportion of the deformation is
904 taken up by folding (Figure 17b), uncertainties are higher due to challenges in interpreting
905 continuous cut-offs. These challenges are related to the variability of the horizon dip, the
906 distance to the inflection point and the variability and magnitude of fault dip. Finally,
907 uncertainties were particularly evident in complex fault zones (Figure 17c), where the image
908 quality may be more degraded and there may be challenges in interpreting deformation
909 across multiple nearby fault strands. The factors shown in Figure 17 indicate why there are
910 along-strike and down-dip variations in the uncertainties, and therefore highlights that
911 there may be local geometric variations in fault geometry that merit additional care and
912 quantification of uncertainties.

913 **7 Conclusions**

914 Our study demonstrated that fault properties extracted from seismic reflection datasets are
915 prone to three types of uncertainty: interpretation repeatability, measurement obliquity,
916 and interpreted cut-off type. Obliquity related errors varies depending on the horizon and
917 fault interpreted, the magnitude of obliquity, and the fault property measured. High errors
918 occurred when obliquity exceeded $\pm 20^\circ$, with throw showing lower percentage errors
919 compared to heave across all datasets. Heave errors caused uncertainties in displacement
920 and dip extraction, particularly in areas of low displacement. Repeatability errors were
921 $\sim \pm 10\%$ for throw, and 13-23% for heave, with higher errors in areas of structural complexity
922 or low seismic image quality. Measurement obliquity was not found to compound
923 repeatability errors; however, interpreting continuous cut-offs increased uncertainty and
924 error in extracted fault properties.

925 Measurement obliquity and interpretation repeatability had a minor effect on the
926 calculation of shale gouge ratio (SGR) across SF2, however, significant errors were observed
927 in local fault plane patches. The small difference in SGR is primarily caused by the high
928 Vshale content of the intervening succession. The magnitude of errors will be similar in
929 reservoirs that have a greater sand content and are near the sealing threshold. In these
930 cases, the fault might experience unexpected local cross-fault fluid flow, compromising for
931 example carbon capture and storage facilities. Slip-rate extraction, which utilises continuous
932 cut-offs, was strongly affected by both obliquity and repeatability errors. This could lead to
933 over- or underestimation of slip-rate and differences in the interpreted slip-rate profile,
934 impacting fault-based seismic hazard assessments, especially in low seismicity areas, and
935 therefore the suitability for example of hosting a geological disposal facility for nuclear

936 waste. These examples underline the importance of considering and mitigating obliquity

937 and repeatability errors when extracting fault data from seismic reflection datasets.

938 **References**

- 939 Alcalde, J., Bond, C.E., 2022. Chapter 5 - Subjective uncertainty and biases: The impact on
 940 seismic data interpretation. In: Bell, R., Iacopini, D., Vardy, M. (Eds.), *Interpreting*
 941 *Subsurface Seismic Data*. Elsevier, 103–123. [https://doi.org/10.1016/B978-0-12-](https://doi.org/10.1016/B978-0-12-818562-9.00002-9)
 942 [818562-9.00002-9](https://doi.org/10.1016/B978-0-12-818562-9.00002-9)
- 943 Alcalde, J., Bond, C.E., Johnson, G., Butler, R.W.H., Cooper, M.A., Ellis, J.F., 2017a. The
 944 importance of structural model availability on seismic interpretation. *Journal of*
 945 *Structural Geology* 97, 161–171. <https://doi.org/10.1016/j.jsg.2017.03.003>
- 946 Alcalde, J., Bond, C.E., Johnson, G., Ellis, J.F., Butler, R.W.H., 2017b. Impact of seismic image
 947 quality on fault interpretation uncertainty. *GSA Today*.
 948 <https://doi.org/10.1130/GSATG282A.1>
- 949 Allen, P.A., Allen, J.R., 2013. *Basin Analysis: Principles and Application to Petroleum Play*
 950 *Assessment*. John Wiley & Sons.
- 951 Amonette, J.E., Barr, J.L., Dobeck, L.M., Gullickson, K., Walsh, S.J., 2010. Spatiotemporal
 952 changes in CO₂ emissions during the second ZERT injection, August–September
 953 2008. *Environmental Earth Sciences* 60, 263–272. [https://doi.org/10.1007/s12665-](https://doi.org/10.1007/s12665-009-0402-0)
 954 [009-0402-0](https://doi.org/10.1007/s12665-009-0402-0)
- 955 Andrews, B.J., Roberts, J.J., Shipton, Z.K., Bigi, S., Tartarello, M.C., Johnson, G., 2019. How do
 956 we see fractures? Quantifying subjective bias in fracture data collection. *Solid Earth*
 957 10, 487–516. <https://doi.org/10.5194/se-10-487-2019>
- 958 Bense, V.F., Gleeson, T., Loveless, S.E., Bour, O., Scibek, J., 2013. Fault zone hydrogeology.
 959 *Earth-Science Reviews* 127, 171–192.
 960 <https://doi.org/10.1016/j.earscirev.2013.09.008>
- 961 Bilal, A., McClay, K., 2022. Tectonic and stratigraphic evolution of the central Exmouth
 962 Plateau, NW Shelf of Australia. *Marine and Petroleum Geology* 136.
 963 <https://doi.org/10.1016/j.marpetgeo.2021.105447>
- 964 Bilal, A., McClay, K., Scarselli, N., 2020. Fault-scarp degradation in the central Exmouth
 965 Plateau, North West Shelf, Australia. *Geological Society, London, Special Publications*
 966 476, 231–257. <https://doi.org/10.1144/SP476.11>
- 967 Black, M., McCormack, K.D., Elders, C., Robertson, D., 2017. Extensional fault evolution
 968 within the Exmouth Sub-basin, North West Shelf, Australia. *Marine and Petroleum*
 969 *Geology* 85, 301–315. <https://doi.org/10.1016/j.marpetgeo.2017.05.022>
- 970 Bond, C.E., 2015. Uncertainty in structural interpretation: Lessons to be learnt. *Journal of*
 971 *Structural Geology* 74, 185–200. <https://doi.org/10.1016/j.jsg.2015.03.003>
- 972 Bond, C.E., Gibbs, A.D., Shipton, Z.K., Jones, S., 2007. What do you think this is? “Conceptual
 973 uncertainty” in geoscience interpretation. *GSA Today* 17, 4.
 974 <https://doi.org/10.1130/GSAT01711A.1>
- 975 Bond, C.E., Lunn, R.J., Shipton, Z.K., Lunn, A.D., 2012. What makes an expert effective at
 976 interpreting seismic images? *Geology* 40, 75–78. <https://doi.org/10.1130/G32375.1>
- 977 Brown, A.R., 2011. *Interpretation of Three-Dimensional Seismic Data*, 7th ed. American
 978 Association of Petroleum Geologists.
- 979 Chellingsworth, L., Bentley, M., Wynn, T., 2015. Human factors in seismic uncertainty —
 980 Restoring a realistic uncertainty range. *Interpretation* 3, SQ21–SQ32.
 981 <https://doi.org/10.1190/INT-2014-0203.1>
- 982 Childs, C., Manzocchi, T., Nicol, A., Walsh, J.J., Soden, A.M., Conneally, J.C., Delogkos, E.,
 983 2017. The relationship between normal drag, relay ramp aspect ratio and fault zone

984 structure. Geological Society, London, Special Publications 439, 355–372.
985 <https://doi.org/10.1144/SP439.16>

986 Childs, C., Manzocchi, T., Walsh, J.J., Bonson, C.G., Nicol, A., Schöpfer, M.P.J., 2009. A
987 geometric model of fault zone and fault rock thickness variations. *Journal of*
988 *Structural Geology* 31, 117–127. <https://doi.org/10.1016/j.jsg.2008.08.009>

989 Choi, J.-H., Edwards, P., Ko, K., Kim, Y.-S., 2016. Definition and classification of fault damage
990 zones: A review and a new methodological approach. *Earth-Science Reviews* 152,
991 70–87. <https://doi.org/10.1016/j.earscirev.2015.11.006>

992 Connor, C.B., Chapman, N.A., Connor, L.J., 2009. *Volcanic and Tectonic Hazard Assessment*
993 *for Nuclear Facilities*. Cambridge University Press.

994 Cowie, P.A., Underhill, J.R., Behn, M.D., Lin, J., Gill, C.E., 2005. Spatio-temporal evolution of
995 strain accumulation derived from multi-scale observations of Late Jurassic rifting in
996 the northern North Sea: A critical test of models for lithospheric extension. *Earth and*
997 *Planetary Science Letters* 234, 401–419. <https://doi.org/10.1016/j.epsl.2005.01.039>

998 Delogkos, E., Manzocchi, T., Childs, C., Sachanidis, C., Barbas, T., Schöpfer, M.P.J.,
999 Chatzipetros, A., Pavlides, S., Walsh, J.J., 2017. Throw partitioning across normal
1000 fault zones in the Ptolemais Basin, Greece. Geological Society, London, Special
1001 Publications 439, 333–353. <https://doi.org/10.1144/SP439.19>

1002 Delogkos, E., Saqab, M.M., Walsh, J.J., Roche, V., Childs, C., 2020. Throw variations and
1003 strain partitioning associated with fault-bend folding along normal faults. *Solid Earth*
1004 11, 935–945. <https://doi.org/10.5194/se-11-935-2020>

1005 Direen, N.G., Stagg, H.M.J., Symonds, P.A., Colwell, J.B., 2008. Architecture of volcanic rifted
1006 margins: new insights from the Exmouth – Gascoyne margin, Western Australia.
1007 *Australian Journal of Earth Sciences* 55, 341–363.
1008 <https://doi.org/10.1080/08120090701769472>

1009 Faleide, T.S., Braathen, A., Lecomte, I., Mulrooney, M.J., Midtkandal, I., Bugge, A.J., Planke,
1010 S., 2021. Impacts of seismic resolution on fault interpretation: Insights from seismic
1011 modelling. *Tectonophysics* 816, 229008.
1012 <https://doi.org/10.1016/j.tecto.2021.229008>

1013 Fenton, C.H., Adams, J., Halchuk, S., 2006. Seismic Hazards Assessment for Radioactive
1014 Waste Disposal Sites in Regions of Low Seismic Activity. *Geotechnical & Geological*
1015 *Engineering* 24, 579–592. <https://doi.org/10.1007/s10706-005-1148-4>

1016 Frodeman, R., 1995. Geological reasoning: Geology as an interpretive and historical science.
1017 *Geological Society of America Bulletin* 107, 960–968. [https://doi.org/10.1130/0016-](https://doi.org/10.1130/0016-7606(1995)107<0960:GRGAAI>2.3.CO;2)
1018 [7606\(1995\)107<0960:GRGAAI>2.3.CO;2](https://doi.org/10.1130/0016-7606(1995)107<0960:GRGAAI>2.3.CO;2)

1019 Gambino, S., Barreca, G., Gross, F., Monaco, C., Gutscher, M.-A., Alsop, G.I., 2022. Assessing
1020 the rate of crustal extension by 2D sequential restoration analysis: A case study from
1021 the active portion of the Malta Escarpment. *Basin Research* 34, 321–341.
1022 <https://doi.org/10.1111/bre.12621>

1023 Gartrell, A., Torres, J., Dixon, M., Keep, M., Gartrell, A., Torres, J., Dixon, M., Keep, M., 2016.
1024 Mesozoic rift onset and its impact on the sequence stratigraphic architecture of the
1025 Northern Carnarvon Basin. *The APPEA Journal* 56, 143–158.
1026 <https://doi.org/10.1071/AJ15012>

1027 Gibson, R.G., Bentham, P.A., 2003. Use of fault-seal analysis in understanding petroleum
1028 migration in a complexly faulted anticlinal trap, Columbus Basin, offshore Trinidad.
1029 *AAPG Bulletin* 87, 465–478. <https://doi.org/10.1306/08010201132>

1030 Goodman, S.N., 2016. Aligning statistical and scientific reasoning. *Science* 352, 1180–1181.
1031 <https://doi.org/10.1126/science.aaf5406>

1032 IPCC, 2005. *Carbon Dioxide Capture and Storage*. Cambridge University Press, Cambridge,
1033 UK.

1034 Jackson, C.A.-L., Rotevatn, A., 2013. 3D seismic analysis of the structure and evolution of a
1035 salt-influenced normal fault zone: A test of competing fault growth models. *Journal*
1036 *of Structural Geology* 54, 215–234. <https://doi.org/10.1016/j.jsg.2013.06.012>

1037 Karner, G.D., Driscoll, N.W., 1999. Style, timing and distribution of tectonic deformation
1038 across the Exmouth Plateau, northwest Australia, determined from stratal
1039 architecture and quantitative basin modelling. In: MacNiocall, C., Ryan, P. (Eds.),
1040 *Continental Tectonics, Proceedings of the Ocean Drilling Program*. Geological Society
1041 of London, London, UK, 271–311. <https://doi.org/10.2973/odp.proc.sr.122.1992>

1042 Klusman, R.W., 2003. A geochemical perspective and assessment of leakage potential for a
1043 mature carbon dioxide-enhanced oil recovery project and as a prototype for carbon
1044 dioxide sequestration; Rangely field, Colorado. *AAPG Bulletin* 87, 1485–1507.
1045 <https://doi.org/10.1306/04220302032>

1046 Lathrop, B.A., Jackson, C.A.-L., Bell, R.E., Rotevatn, A., 2021. Normal Fault Kinematics and
1047 the Role of Lateral Tip Retreat: An Example From Offshore NW Australia. *Tectonics*
1048 40, e2020TC006631. <https://doi.org/10.1029/2020TC006631>

1049 Magee, C., Jackson, C.A.-L., 2020a. Can we relate the surface expression of dike-induced
1050 normal faults to subsurface dike geometry? *Geology* 49, 366–371.
1051 <https://doi.org/10.1130/G48171.1>

1052 Magee, C., Jackson, C.A.-L., 2020b. Seismic reflection data reveal the 3D structure of the
1053 newly discovered Exmouth Dyke Swarm, offshore NW Australia. *Solid Earth* 11, 579–
1054 606. <https://doi.org/10.5194/se-11-579-2020>

1055 Magee, C., Love, V., Fayez, K., Andrews, B., Rivas-Dorado, S., Jackson, C., Orlov, C.,
1056 Bramham, E., 2023. Quantifying Dyke-Induced Graben and Dyke Structure Using 3D
1057 Seismic Reflection Data and The Role of Interpretation Bias. *Tektonika* 1, 32–53.
1058 <https://doi.org/10.55575/tektonika2023.1.2.25>

1059 Magee, C., Love, V., Fayez, K., Andrews, B., Rivas-Dorado, S., Jackson, C.A.-L., Orlov, C.,
1060 Bramham, E.K., in review. Quantifying dyke-induced graben and dyke structure using
1061 3D seismic reflection data. *Tektonika*.

1062 Marsh, N., Imber, J., Holdsworth, R.E., Brockbank, P., Ringrose, P., 2010. The structural
1063 evolution of the Halten Terrace, offshore Mid-Norway: extensional fault growth and
1064 strain localisation in a multi-layer brittle–ductile system. *Basin Research* 22, 195–
1065 214. <https://doi.org/10.1111/j.1365-2117.2009.00404.x>

1066 Meyer, V., Nicol, A., Childs, C., Walsh, J.J., Watterson, J., 2002. Progressive localisation of
1067 strain during the evolution of a normal fault population. *Journal of Structural*
1068 *Geology* 24, 1215–1231. [https://doi.org/10.1016/S0191-8141\(01\)00104-3](https://doi.org/10.1016/S0191-8141(01)00104-3)

1069 Michie, E.A.H., Mulrooney, M.J., Braathen, A., 2021. Fault Interpretation Uncertainties using
1070 Seismic Data, and the Effectson Fault Seal Analysis: A Case Study from the Horda
1071 Platform, withImplications for CO₂</sub> storage. preprint.
1072 Tectonic plate interactions, magma genesis, and lithosphere deformation at all
1073 scales/Structural geology and tectonics, rock physics, experimental
1074 deformation/Structural geology. <https://doi.org/10.5194/se-2021-23>

1075 Miocic, J.M., Johnson, G., Gilfillan, S.M.V., 2014. Fault seal analysis of a natural CO₂
1076 reservoir in the Southern North Sea. *Energy Procedia*, 12th International Conference

1077 on Greenhouse Gas Control Technologies, GHGT-12 63, 3364–3370.
1078 <https://doi.org/10.1016/j.egypro.2014.11.365>

1079 Mörner, N.-A., 2013. Patterns in seismology and palaeoseismology, and their application in
1080 long-term hazard assessments – the Swedish case in view of nuclear waste
1081 management. *Pattern Recognition in Physics* 1, 75–89. [https://doi.org/10.5194/prp-](https://doi.org/10.5194/prp-1-75-2013)
1082 [1-75-2013](https://doi.org/10.5194/prp-1-75-2013)

1083 Nicol, A., Walsh, J., Berryman, K., Nodder, S., 2005. Growth of a normal fault by the
1084 accumulation of slip over millions of years. *Journal of Structural Geology* 27, 327–
1085 342. <https://doi.org/10.1016/j.jsg.2004.09.002>

1086 Osagiede, E.E., Duffy, O.B., Jackson, C.A.-L., Wrona, T., 2014. Quantifying the growth history
1087 of seismically imaged normal faults. *Journal of Structural Geology* 66, 382–399.
1088 <https://doi.org/10.1016/j.jsg.2014.05.021>

1089 Pan, S., Bell, R.E., Jackson, C.A.-L., Naliboff, J., 2021. Evolution of normal fault displacement
1090 and length as continental lithosphere stretches. *Basin Research* 34, 121–140.
1091 <https://doi.org/10.1111/bre.12613>

1092 Pan, S., Naliboff, J., Bell, R., Jackson, C., 2022. Bridging Spatiotemporal Scales of Normal
1093 Fault Growth During Continental Extension Using High-Resolution 3D Numerical
1094 Models. *Geochemistry, Geophysics, Geosystems* 23, e2021GC010316.
1095 <https://doi.org/10.1029/2021GC010316>

1096 Paumard, V., Bourget, J., Payenberg, T., Ainsworth, R.B., George, A.D., Lang, S., Posamentier,
1097 H.W., Peyrot, D., 2018. Controls on shelf-margin architecture and sediment
1098 partitioning during a syn-rift to post-rift transition: Insights from the Barrow Group
1099 (Northern Carnarvon Basin, North West Shelf, Australia). *Earth-Science Reviews* 177,
1100 643–677. <https://doi.org/10.1016/j.earscirev.2017.11.026>

1101 Pérez-Díaz, L., Alcalde, J., Bond, C.E., 2020. Introduction: Handling uncertainty in the
1102 geosciences: identification, mitigation and communication. *Solid Earth* 11, 889–897.
1103 <https://doi.org/10.5194/se-11-889-2020>

1104 Reeve, M.T., Jackson, C.A.-L., Bell, R.E., Magee, C., Bastow, I.D., 2016. The stratigraphic
1105 record of prebreakup geodynamics: Evidence from the Barrow Delta, offshore
1106 Northwest Australia. *Tectonics* 35, 1935–1968.
1107 <https://doi.org/10.1002/2016TC004172>

1108 Reeve, M.T., Magee, C., Bastow, I.D., McDermott, C., Jackson, C.A.-L., Bell, R.E., Prytulak, J.,
1109 2021. Nature of the Cuvier Abyssal Plain crust, offshore NW Australia. *Journal of the*
1110 *Geological Society* 178, jgs2020-172. <https://doi.org/10.1144/jgs2020-172>

1111 Robb, M.S., Taylor, B., Goodliffe, A.M., 2005. Re-examination of the magnetic lineations of
1112 the Gascoyne and Cuvier Abyssal Plains, off NW Australia. *Geophysical Journal*
1113 *International* 163, 42–55. <https://doi.org/10.1111/j.1365-246X.2005.02727.x>

1114 Robledo Carvajal, F., Butler, R.W.H., Bond, C.E., 2023. Mapping faults in 3D seismic data –
1115 why the method matters. *Journal of Structural Geology* 104976.
1116 <https://doi.org/10.1016/j.jsg.2023.104976>

1117 Roche, V., Camanni, G., Childs, C., Manzocchi, T., Walsh, J., Conneally, J., Saqab, M.M.,
1118 Delogkos, E., 2021. Variability in the three-dimensional geometry of segmented
1119 normal fault surfaces. *Earth-Science Reviews* 216, 103523.
1120 <https://doi.org/10.1016/j.earscirev.2021.103523>

1121 Rodríguez-Salgado, P., Childs, C., Shannon, P.M., Walsh, J.J., 2023. Influence of basement
1122 fabrics on fault reactivation during rifting and inversion: a case study from the Celtic

1123 Sea basins, offshore Ireland. *Journal of the Geological Society* 180, jgs2022-024.
1124 <https://doi.org/10.1144/jgs2022-024>

1125 Schaaf, A., Bond, C.E., 2019. Quantification of uncertainty in 3-D seismic interpretation:
1126 implications for deterministic and stochastic geomodeling and machine learning.
1127 *Solid Earth* 10, 1049–1061. <https://doi.org/10.5194/se-10-1049-2019>

1128 Shipton, Z.K., Cowie, P.A., 2003. A conceptual model for the origin of fault damage zone
1129 structures in high-porosity sandstone. *Journal of Structural Geology* 25, 333–344.
1130 [https://doi.org/10.1016/S0191-8141\(02\)00037-8](https://doi.org/10.1016/S0191-8141(02)00037-8)

1131 Shipton, Z.K., Roberts, J.J., Comrie, E.L., Kremer, Y., Lunn, R.J., Caine, J.S., 2020. Fault
1132 fictions: systematic biases in the conceptualization of fault-zone architecture.
1133 *Geological Society, London, Special Publications* 496, 125–143.
1134 <https://doi.org/10.1144/SP496-2018-161>

1135 Stagg, H., Alcock, M., Bernardel, G., Moore, A., Symonds, P., Exon, N., 2004. Geological
1136 framework of the outer Exmouth Plateau and adjacent ocean basins. *Geoscience*
1137 *Australia*.

1138 Steventon, M.J., Jackson, C.A.-L., Hall, M., Ireland, M.T., Munafo, M., Roberts, K.J., 2022.
1139 Reproducibility in Subsurface Geoscience. *Earth Science, Systems and Society* 2,
1140 10051. <https://doi.org/10.3389/esss.2022.10051>

1141 Tannert, C., Elvers, H.-D., Jandrig, B., 2007. The ethics of uncertainty. *EMBO Reports* 8, 885–
1142 974. <https://doi.org/10.1038/sj.embor.7401072>

1143 Taylor, S.K., Nicol, A., Walsh, J.J., 2008. Displacement loss on growth faults due to sediment
1144 compaction. *Journal of Structural Geology* 30, 394–405.
1145 <https://doi.org/10.1016/j.jsg.2007.11.006>

1146 Terzaghi, R.D., 1965. Sources of Error in Joint Surveys. *Géotechnique* 15, 287–304.
1147 <https://doi.org/10.1680/geot.1965.15.3.287>

1148 Tindale, K., Newell, N., Keall, J., Smith, N., 1998. Abstract: Structural Evolution and Charge
1149 History of the Exmouth Sub-Basin Northern Carnarvon Basin, Offshore Western
1150 Australia.

1151 Watkins, H., Bond, C.E., Healy, D., Butler, R.W.H., 2015. Appraisal of fracture sampling
1152 methods and a new workflow to characterise heterogeneous fracture networks at
1153 outcrop. *Journal of Structural Geology* 72, 67–82.
1154 <https://doi.org/10.1016/j.jsg.2015.02.001>

1155 Yang, X.-M., Elders, C., 2016. The Mesozoic structural evolution of the Gorgon Platform,
1156 North Carnarvon Basin, Australia. *Australian Journal of Earth Sciences* 63, 755–770.
1157 <https://doi.org/10.1080/08120099.2016.1243579>

1158 Yielding, G., 2002. Shale Gouge Ratio — calibration by geohistory. In: Koestler, A.G.,
1159 Hunsdale, R. (Eds.), *Norwegian Petroleum Society Special Publications, Hydrocarbon*
1160 *Seal Quantification*. Elsevier, 1–15. [https://doi.org/10.1016/S0928-8937\(02\)80003-0](https://doi.org/10.1016/S0928-8937(02)80003-0)

1161 Yielding, G., Lykakis, N., Underhill, J.R., 2011. The role of stratigraphic juxtaposition for seal
1162 integrity in proven CO₂ fault-bound traps of the Southern North Sea. *Petroleum*
1163 *Geoscience* 17, 193–203. <https://doi.org/10.1144/1354-0793/10-026>

1164